Master Thesis

Unraveling the Transitional Disk RX J1615.3-3255: Scattered Light Observations Versus Disk Models

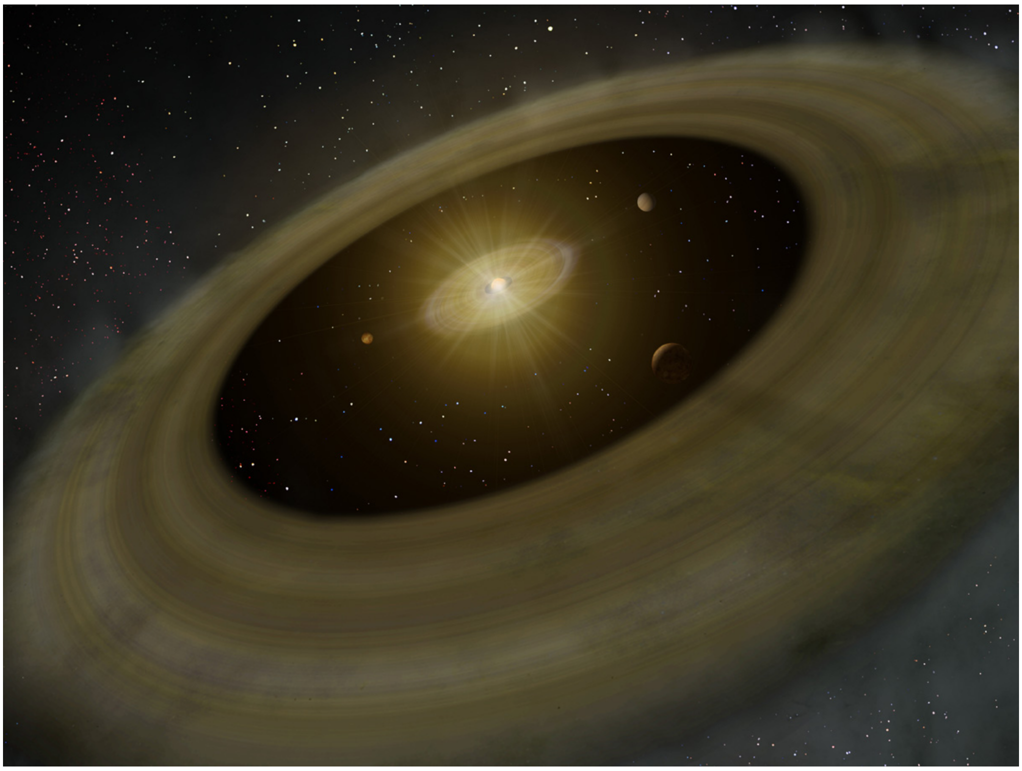

Author:
Robin Kooistra

Supervisors:
Prof. dr. Inga Kamp
Prof. Misato Fukagawa

July 15, 2014

Image credit: NAOJ

Abstract

We present a two-stage analysis of the transitional disk RX J1615.3-3255 located in the Lupus association (∼1 Myr old). Using 1.6 μm scattered light, polarized intensity images observed with the HiCIAO instrument of the Subaru Telescope, we deduce the position angle and the inclination angle. The disk is found to extend out to 92 ± 12 AU in the scattered light and no clear structure is observed, nor do we see a central decrease in intensity seen in $880 \mu m$ continuum observations from the literature. We then analyse two different disk models that are based on the Spectral Energy Distribution (SED). We construct a single-zone, continuous disk model and a multi-zone model with a cavity at 30 AU and a puffed up cavity wall. From these models, we produce simulated images to compare with our observations and submm images from the literature. The multi-zone disk model gives the best reproduction of the observations. Both models show stability against self-gravitation throughout the entire disk, assuming a gas-to-dust ratio of 100. Therefore, the formation of planets through a gravitational instability is unlikely in these models.

Contents

Chapter 1

Introduction & Theory

Ever since the discovery of the planets in our Solar System, scientists have been curious to find out how it formed and if planetary systems like our own also exist around other stars. With the number of observations of exoplanets having been steadily increasing over the course of the last decade [1], the search for the mechanisms behind planet formation has also been gaining popularity.

1.1 Protoplanetary Disks in Perspective

Currently, planets are believed to form inside protoplanetary disks [2]. As a star is formed from the gravitational collapse of a rotating cloud clore of molecular gas, material with high angular momentum compared to the inner regions, falls inward. The conservation of angular momentum forces the material into a circumstellar disk, the size of which depends on the initial properties of the core [3]. It consists of both dust and gas of a few percent of the stellar mass. These disks have been directly observed around young stars ($\sim$ few million years) in nearby star forming regions (see Figure 1.1). Disk sizes measured in the Orion nebula range from 50 to $\sim$ 200 AU in radius [4].

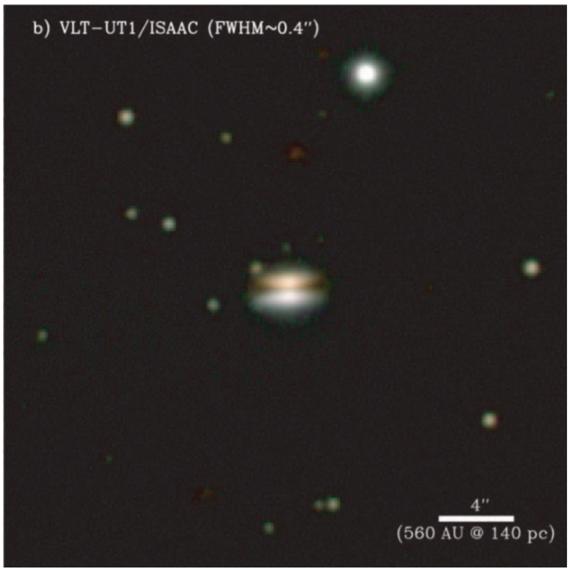

Figure 1.1: J, H and K_s band composite image of the protoplanetary disk 2MASSI J1628137-243139 in scattered light [5].

These disks evolve rapidly on Myr timescales from optically thick disks into optically thin debris disks where most of the material has been dispersed, possibly harboring a planetary system [3]. The evolution of protoplanetary disks is governed by both viscous accretion, responsible for the transport of angular momentum, and photoevaporation by a strong ultra-violet (UV) or X-ray radiation source [2].
Protoplanetary disks are thought to be the birthplace of planets because most of the planets in our Solar System orbit the Sun in the same orbital plane and the same direction, supporting the idea that they have formed from a rotating disk around the star. There are two main scenarios through wich they are believed to form within the disk [2]. The dust grains in the disk can collide and in the process stick together, creating a larger dust grain. Dust grains are thought to eventually grow into kilometer sized planetesimals, which are so massive that gravity becomes important enough for it to start affecting its environment, attracting dust and gas in its surroundings [2]. The second scenario relies on the disk being massive enough for it to become gravitationally unstable. This causes the disk to fragment and form gas giant planets [2].
Studying the gas and dust in protoplanetary disks can therefore be instrumental in learning how planetary systems like our own are able to form.

1.2 Spectral Energy Distribution & Lada Classification

One of the tools that can be used to study the structure of the dust in a protoplanetary disk is the so-called *Spectral Energy Distribution*, or SED. It is usually given by the specific flux ($\lambda \cdot F_\lambda$ or $\nu \cdot F_\nu$) as a function of wavelength or frequency [2]. Different types of objects have different energy outputs at different wavelengths. For young stellar objects (YSOs), there are typically two components that supply the emission. The stellar component (in this case the protostar) can be approximated as a blackbody in the SED (see Figure 1.2a), for which the position of the peak depends on the stellar type and thus the effective temperature. This photospheric spectrum usually peaks at wavelengths around $\sim 1\mu m$ for $\lesssim 2M_\odot$ pre-main sequence stars [3]. Furthermore, YSOs show emission at infrared (IR) wavelengths that is above the photospheric level. This is thermal emission coming from the dust in the circumstellar disk. The warmer the dust, the lower the wavelength at which it emits. Therefore, the material closest to the star would emit in the near-IR (1-5 μm), moving outwards to the mid-IR (5-20 μm) and submm for the colder dust. This also correlates with the size of the dust grains, as the thermal emission from larger grains dominates at larger wavelengths, making the submm part of the SED most sensitive to the disk dust mass. The temperature dependence is shown schematically in Figure 1.2b where each color represents a section of the disk which emits thermally at a different temperature.

Because of these characteristics, YSOs can be classified based on the features of their IR-excess [2]. The generally used convention is to divide the young stellar objects into four classes ranging from class 0 to class III based on the slope of the IR-SED. This is known as the Lada classification, named after Charles Lada, who introduced Classes I through III in 1987 [7]. The Class 0 objects were added after their discovery by Andre et al. [8]. This classification, although emperically determined, can also be interpreted as an evolutionary sequence.

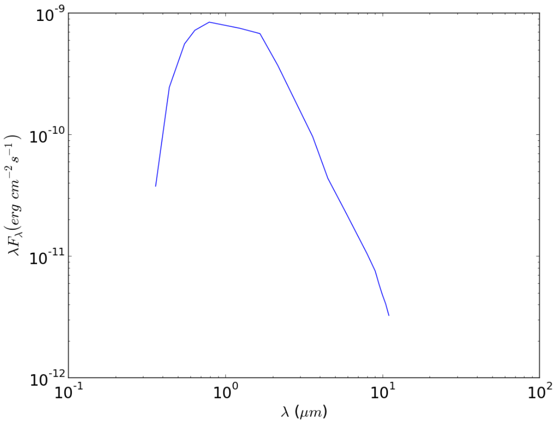

(a) Purely photospheric SED.

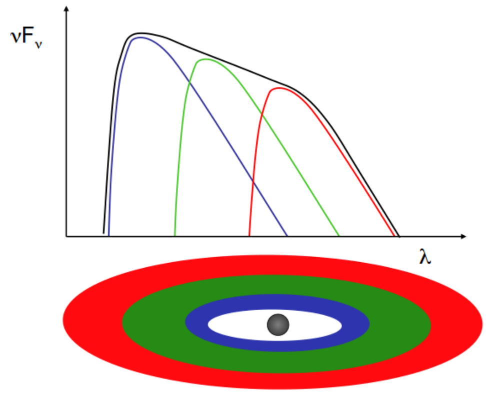

(b) Different sections of a circumstellar disk have different temperatures. Each color corresponds to a temperature zone from hot (blue) to cold (red) [6].

Figure 1.2: Different contributions to the Spectral Energy Distribution (SED)

Figure 1.3 gives sketches of the different evolutionary stages (left) and their corresponding SEDs (right). The stages are thought to represent the following:

- **Class 0**: This is the youngest class of objects. An optically thick core is deeply embedded in an accreting envelope. All the light of the protostar forming in the core is obscured and thus the SED peaks in the mid- to far-IR (20 μm-1 mm). These objects are not visible in the optical.

- **Class I**: The star becomes partially visible in the optical as the surrounding envelope becomes less optically thick. This class can have outflows and jets. It is also the class where a circumstellar disk forms. In the SED, the emission at optical wavelengths starts to appear and the overall emission moves more towards the mid-IR as the circumstellar disks emission becomes more important.

- **Class II**: The star has become completely visible as the envelope has dissipated. It is now surrounded by an optically thick accretion disk. The SED is a combination of photospheric emission, together with a strong IR-excess coming from the disk.

- **Class III**: The disk itself has dissipated, leaving only a pre-main-sequence star and possibly a planetary system or an optically thin debris disk. The SED is now dominated completely by photospheric emission and possibly a very small excess at larger wavelengths.

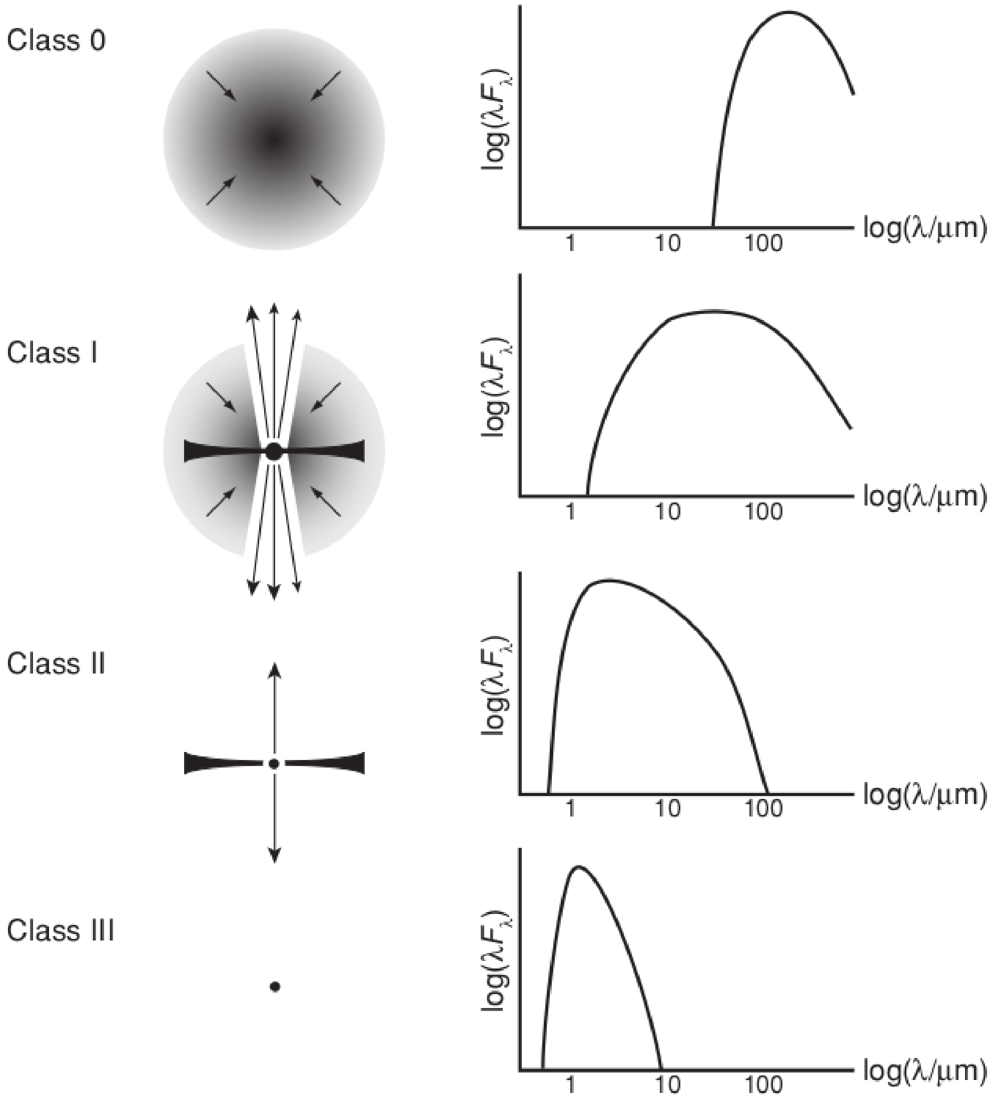

Figure 1.3: The Lada classification scheme depicting the different evolutionary stages of YSOs (left) and the corresponding typical SED shape (right) [2].

As with many classification systems, the Lada classification is not necessarily representative for the full range of observations as sometimes objects cannot be clearly put into one of these classes. This is where the so-called transitional disks come into play.

1.3 Transitional disks

Transitional disks are objects that, in terms of their SED, falls in between Class II and Class III. They exhibit almost no near-IR excess, yet harbor a strong mid- and far-IR excess [9]. The former suggests that the inner regions have been cleared of material, forming a hole in the disk. Strom et al. [10] suggested that they are a transition stage in the evolution from an optically thick disk extending towards the star into a dispersed low-mass disk. Another possibility is that the SED does have a near-IR excess, but a dip in the mid-IR part of the SED. These can be interpreted as a two disk system that has a gap in between [11]. These are sometimes refered to as pre-transitional disks [9]. A schematic of the structure of the different disk types is given in Figure 1.4.

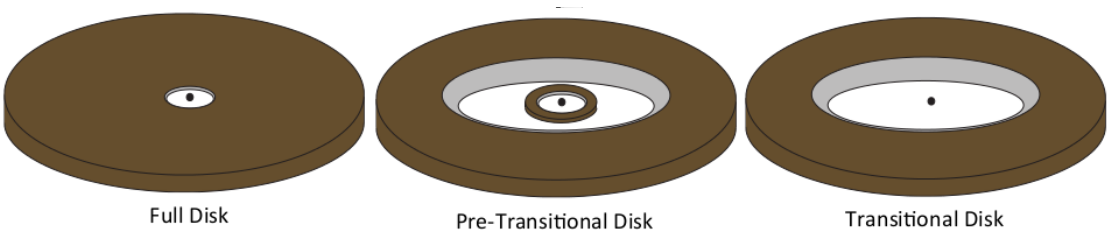

Figure 1.4: Sketch showing the difference between a full, a pre-transitional and a transitional disk. Pre-transitional disks are characterized by a gap, whereas transitional have a large inner hole [9].

A key question that comes to mind for these objects is how their inner region is cleared out. Several mechanisms have been proposed for this [9]. Due to viscosity in disks, they are expected to become optically thin as they accrete[2], but this is a slow process. An alternative is photo-evaporation where material in the surface is heated strongly by the UV or X-ray radiation from the central star, causing an outflow of material from the disk [2]. This cuts off the supply of disk material from the outer disk, making it possible to clear out the inner disk as the material quickly accretes onto the star. A substantial sample of transitional disks, however, show too large inner holes together with too high accretion rates to be explained by photoevaporation alone [12].
It is also possible to create gaps in the disk by dynamical interaction with a massive object [9]. The obvious candidate for this type of clearing is a planetary body, carving a hole by sweeping up material as it moves through the disk. Although no detections of planets within disks have been confirmed yet, the transitional disks are thought to be an important stage in undestanding planet formation [9].

1.4 Polarization in Disks

Part of the stellar emission is scattered by the dust grains in the disk and becomes polarized. This light comes from the surface of the disk if the disk is optically thick and it is able to trace detailed structures, such as spiral arms [13]. The reason this light is polarized follows from the scattering mechanism by dust grains [14]. When an incident light wave (a plane electromagnetic wave) hits a dust grain, the electric field of the light ray causes the electrons in the grain to slightly vibrate along the direction of the field. Because the electric field oscillates perpendicular to the propagation direction of the field, the dust grain will also start emitting radiation in a dipole pattern perpendicular to the direction of the incident light wave. Therefore, this scattered light will be polarized depending on the direction from which the observer views the dust grain. Figure 1.5 shows how two incoming waves with perpendicular linear polarization result in scattered light linearly polarized in the same direction.

In the case of a protoplanetary disk, the incident light ray will come from the star and will not be polarized, but the scattering mechanism stays the same. It will thus give a superposition of the two options in Figure 1.5. Therefore, whenever we see stellar light scattered by dust in the disk, the polarization should be oriented perpendicular to the direction of the position of the star. This is an important property which we can use to show that our observations are truly looking at the scattered light.

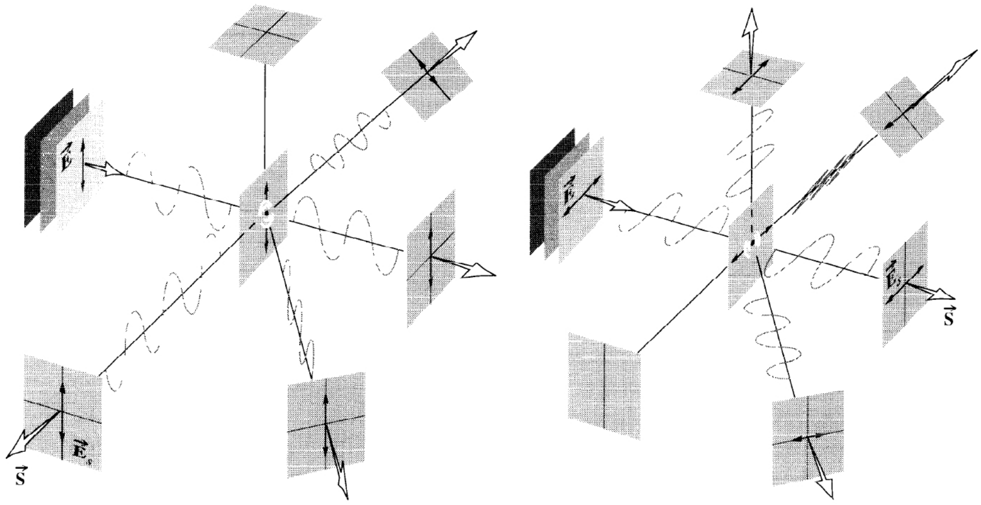

Figure 1.5: Sketch of polarization due to scattering for two orthogonal linearly polarized light waves [14]. The left image begins with a horizontally polarized electric field ($\vec{E}$), whereas the right side begins with a horizontally polarized electic field. $\vec{S}$ gives the propagation direction of the field.

1.4.1 Stokes Parameters

In order to use the properties described above, we need some way to quantify the polarization of the observed light. An option is to use the so-called Stokes parameters [15]. These are four parameters that together can completely describe an electromagnetic wave. Written in terms of the amplitude of the electromagnetic wave A and its phase Δ, the Stokes parameters are defined as:

$$I = \overline{A_x^2 + A_y^2} \tag{1.1}$$
$$Q = \overline{A_x^2 - A_y^2} \tag{1.2}$$
$$U = 2\overline{A_x A_y \cos\Delta} \tag{1.3}$$
$$V = 2\overline{A_x A_y \sin\Delta} \tag{1.4}$$

where A_x and A_y denote the amplitude of two orthogonal axes in the observer plane. I represents the total intensity of the light. Q and U give the degree of linear polarization in two orthogonal directions, whereas V is the circular polarization term. For astronomical situations, V is usually almost equal to 0 due to the mechanism described in Section 1.4 and will therefore be ignored from now on. Because obvervationally one can only measure intensities, rather than the phase and amplitude of the waves, it is much more convenient to use a different convention. Although equivalent to the previous set of equations, in terms of intensities, the Stokes parameters can be rewritten into:

$$I = I_0 + I_{90} \tag{1.5}$$
$$Q = I_0 - I_{90} \tag{1.6}$$
$$U = I_{45} - I_{-45} \tag{1.7}$$

The subscript numbers denote the polarization angle. These are thus relations between intensities of light in two orthogonal polarization states. Later on, in Section 3.2.5 we will go further into combining these equations with actual data. To give the reader better insight into what the Stokes parameters represent, Figure 1.6 shows what having either 100% Stokes Q or 100% Stokes U would mean for the polarization direction.

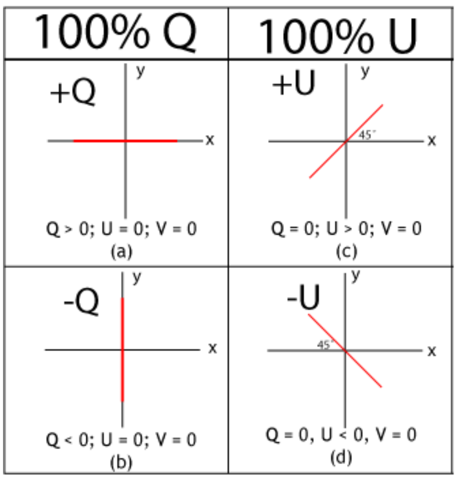

Figure 1.6: Schematic of the ideal cases for only Stokes ±Q or only Stokes ± U. The red line gives the direction of the polarization [16].

With Stokes Q and U we can fully describe the polarization vector using the polarized intensity PI and the polarization angle α through the following relations:

$$PI = \left(Q^2 + U^2\right)^{\frac{1}{2}} \tag{1.8}$$

$$\alpha = \frac{1}{2}\tan^{-1}\left(\frac{U}{Q}\right) \tag{1.9}$$

Combining the polarized intensity with the total intensity (Stokes I) then gives the degree of polarization ($\%_{pol}$ = PI/I), which is a property that depends both on the scattering angle, and the size of the dust [17]. It is also related to the type of dust grains [18]. The relation between $\%_{pol}$ and the scattering angle for compact silicate grains with different grain sizes is shown in Figure 1.7. For the smallest grains, the degree of polarization follows a bell-shaped trend, peaking close to a 90° scattering angle and is not very sensitive to the particle size. The intermediate size particles display a pattern with peaks and ripples due to resonance with the incoming wave as the grain size becomes comparable to the wavelength. The largest grains again show a smooth profile, but with a peak shifted towards $\sim 70°$ because of the increasing importance of forward scattering [18]. So if the degree of polarization can be measured throughout the disk, it is possible to put constraints on the properties and the distribution of dust grains in the disk.

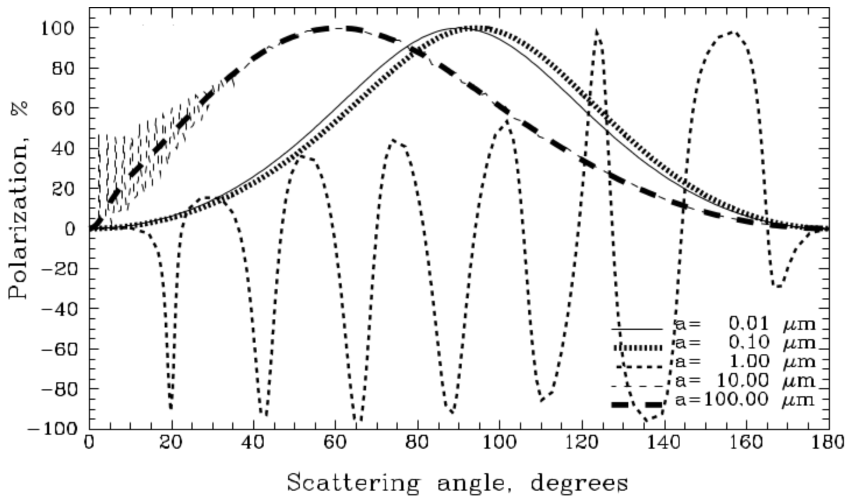

Figure 1.7: Dependence of the degree of polarization on the grain size and scattering angle for compact silicate dust grains at $\lambda = 0.70\mu m$ [17].

1.5 Goal

For this thesis we focus on a single transitional disk, RX J1615.3-3255 and study it in two stages. By means of scattered light observations we want to get constraints on the structure of the disk. This is supplemented by disk modelling based on the SED to get a more complete picture of the RX J1615.3-3255 system. Finally, we create simulated images of these models to compare with our observations. Ultimately, the goal is to get constraints on the planet formation capabilities of RX J1615.3-3255, such as the types of planets that it can form.

Chapter 2

Observing RX J1615.3-3255

Now that theoretical framework has been laid out, we can move on to, quite literally, the star of this thesis. We start with a brief description of some of the work that has already been done in previous studies. Then we introduce the Subaru telescope and the HiCIAO instrument that were used for our own observations of RX J1615.3-3255. Some special observational techniques were applied to this data set that need some explanation. Therefore, we will also spend Sections 2.2.1, 2.2.1 and 2.2.1 on the concepts that are required to be able to understand some of the steps in the data reduction in Chapter 3.

2.1 What Has Been Studied So Far

The transitional disk RX J1615.3-3255 (from here on referred to as RXJ1615) has been studied in a number of papers, going as far back as 1976 [19]. RXJ1615 is located in the constellation Lupus and has been kinematically tied to the young ($\sim$ 1 Myr old) Lupus association at a distance of 185 pc [20]. It was identified as a weak-line T Tauri star by Krautter et al. [21], based on optical spectroscopy. Later in 2010, from Spitzer IR observations, Merín et al. [22] found the first evidence of an inner hole in the disk by performing a fit to the SED, designating it a transitional disk.
Our largest supply of information comes from Andrews et al. [23], who performed high resolution 880 μm observations. Their data, the aperture synthesis map of which can be found in Figure 2.1, clearly shows a decrease in the intensity close to the center. They also ran a disk model to fit both the SED and their submm visibilities. Interestingly, they find a low density cavity out to a radius of 30 AU and a relatively flat, massive disk almost $\sim$ 12% of the stellar mass. We will look into the model in more detail in Chapter 4.

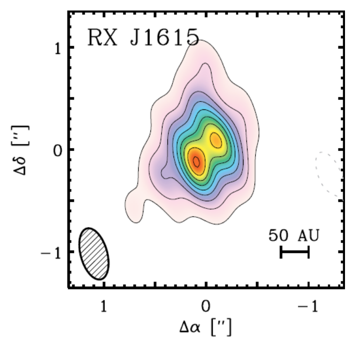

Figure 2.1: 880 μm aperture synthesis map from Andrews et al. [23]. The telescope beam dimensions are shown in the bottom left corner and the contours are drawn at 3σ intervals.

2.2 The Subaru Telecope

For our own observations we used the Subaru Telescope, which is owned by the National Astronomical Observatory of Japan (NAOJ) and is located at the summit of Mauna Kea in Hawaii at an altitude of 4139m [24]. Construction of the telescope was completed in 1998 and it saw first light a year later [25]. It is a Ritchey-Chretien type telescope with an 8.2m primary mirror. This large mirror makes it possible to obtain high angular resolution for the many instruments that can be mounted at the telescope's four foci (see Figure 2.2), covering wavelengths from the near- to mid-IR [26]. The instrument we used for our observations is the High-Contrast Coronographic Imager for Adaptive Optics, or HiCIAO, and is located at the infrared Nasmyth focus of the telescope.

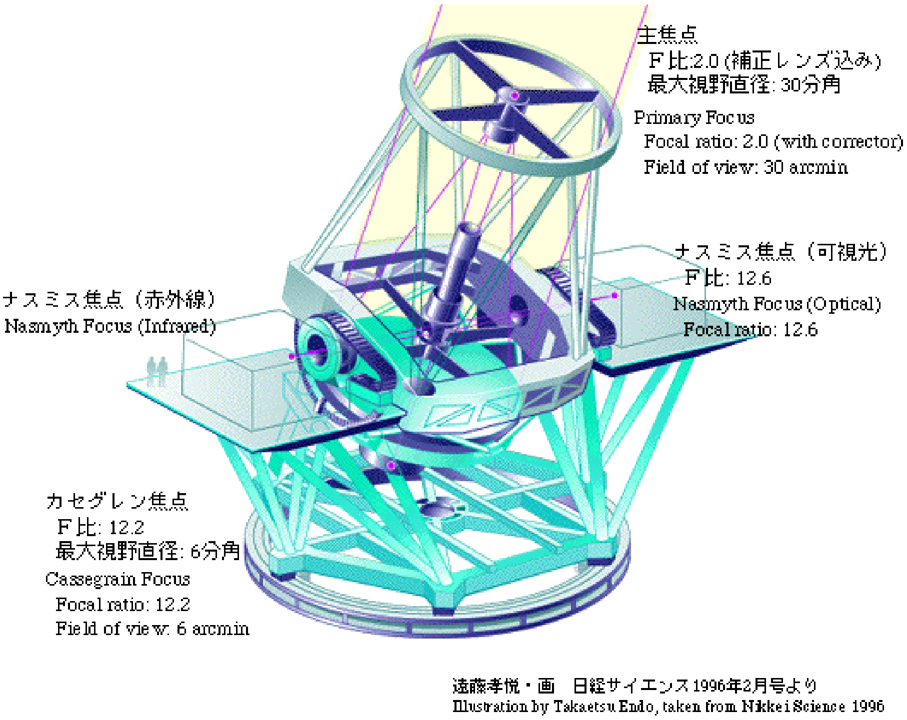

Figure 2.2: Sketch of the Subaru Telescope [24]

2.2.1 HiCIAO and its Observation Modes

Both direct imaging and differential imaging is possible [27]. Together with a Lyot coronograph, which can be used to block the stellar light, HiCIAO is designed for observing circumstellar disks around young stars. HiCIAO is optimized for observing in the H-band, but can observe in the J and K-bands as well [27]. As the name suggests, it is used in conjunction with an adaptive optics (AO) system which corrects the incoming wavefront for atmospheric effects (seeing).
The AO188 system is also mounted on the Nasmyth focus and works with a 188 segment bimorph deformable mirror together with a 188 element curvature wavefront sensor [28]. The incoming light is split into two paths by a beamsplitter. One is sent directly to the detector, whereas the other goes to the wavefront sensor, which then can actively determine how the 188 sections of the deformable mirror should be positioned to correct for the distortion of the wavefront. In order to do this calibration, both a natural and a laser guide star can be used [28]. Together with the AO system, HiCIAO is able to achieve a spatial resolution of 0.04 arcsec in the H-band [27]. Our observations were performed in a combination of two of the observational modes of HiCIAO.

qPDI

The first, and for us most important one is qPDI mode. Here PDI stands for Polarimetric Differential Imaging. This method divides the light into two orthogonal polarization states on the detector using a Wollastan prism together with a rotating half waveplate, simultaneously imaging the two states. In qPDI mode however, the data contains four images of the same source as can be seen in Figure 2.3. The upper row gives the same polarization states as the lower one. Therefore, qPDI mode has the advantage of giving two data sets instantaneously.

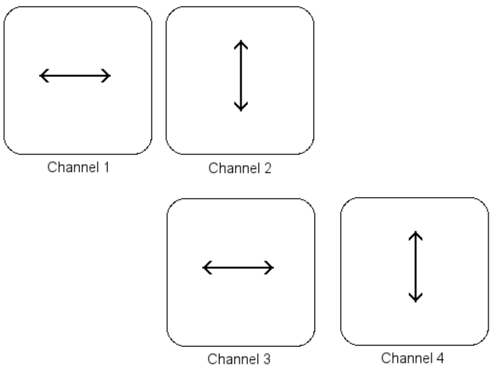

(a) Schematic overview of the qPDI data. The arrows inside the four qPDI windows denote its polarization state. The top and bottom row are identical, giving two data sets.

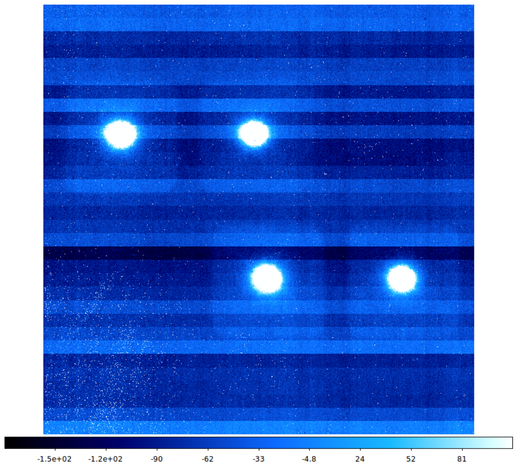

(b) Raw image HICIAO00099889. The numbers underneath the colorbar are given in ADU.

Figure 2.3: qPDI mode data.

Furthermore, the observations are performed in sets of four exposures. Between each image in a single set, the half waveplate is rotated by a certain angle, correpsponding to 0°, 45°, 22.5° and 67.5° respectively. Due the the properties of this instrumental component, the polarization angle then also rotates, but by double the amount of the rotation of the half waveplate itself[15]. Combinations of these different polarization states can then be used to obtain the Stokes parameters following equations 1.5 through 1.7.

Speckle Noise reduction

One of the advantages of PDI is the ability to reduce the amount of speckle noise coming from the high luminosity of the the star compared to the disk, which arise due to uncorrected abberrations of the incoming wavefront [29]. Subtracting a qPDI window with a 0 degree polarization state from one with a polarization of 90 degrees would give a measure of Stokes +Q as was shown in equation 1.6. Rotating the polarization states by 90 degrees (or rotating the half waveplate by 45 degrees) and subtracting the same two channels again would then give Stokes -Q. In this image, the observed object would now have negative pixel values, whereas the speckle noise would be the same as in the +Q image. Therefore, subtracting -Q from +Q should give a $2 \cdot Q$ image with only the physical object and without the speckle noise, which can then be divided by a factor of two. An example of this is given in Figure 2.4. The same process can also be repeated for Stokes U with the 45 and -45 degree polarization states.

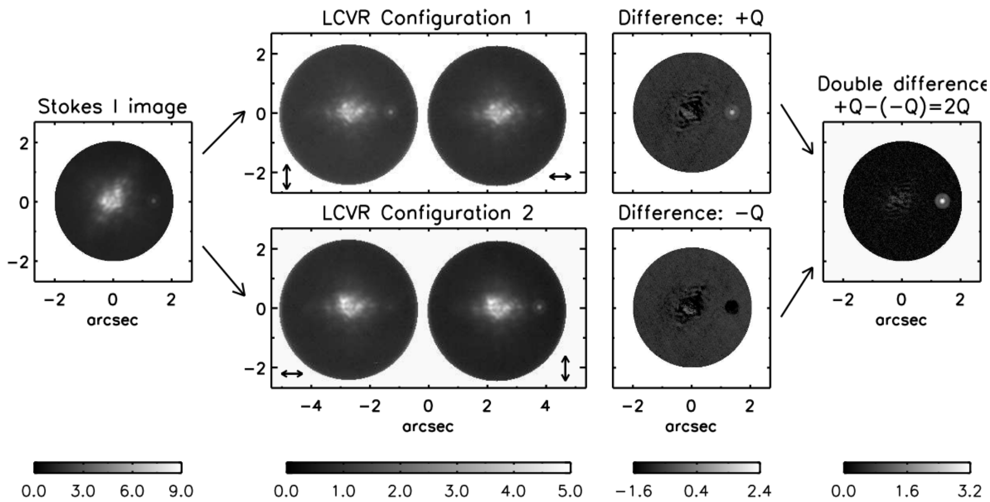

Figure 2.4: Speckle reduction process for Stokes Q. [29] Here Liquid Crystal Variable Retarders (LCVR) were used to obtain the two orthogonal polarization states. Subtracting these images in different LCVR configurations (similar to the half waveplate used in our observations) give both +Q and -Q and then the double difference gives a final Stokes Q image with reduced speckle noise.

ADI

Besides observations of the polarized light from the disk, there is also an interest in directly observing planets. Therefore, our observations were performed in qPDI mode combined with Angular Differential Imaging (ADI) mode. Faint objects around the central star are usually overwhelmed by the strong light coming from the stellar halo. The stellar light thus needs to be subtracted in order to get a clear view of its surroundings. ADI can be a useful tool for this.
During ADI observations, the field of view is rotated around the star. This can be done by exploiting the Earth's own rotation [30]. Because the night sky rotates as time passes during observations, the telescope needs to track the star. If the pupil of the telescope always remains fixed and oriented towards the zenith, whereas the sky itself rotates together with the celestial sphere, the net effect is a difference between the orientation of the object and the orientation of the telescope. A sketch of this situation is shown in Figure 2.5. The result is an inherent rotation of the field in the image as time progresses, where the amount of rotation depends on the position of the object on the sky. The angle can thus be calculated using the celestial coordinates of the object. When the object is at its highest point, the field will rotate the fastest, so depending on how much rotation is desired the observations can be planned accordingly.

Taking the median of the rotated frames will keep the parts that are consistent in all the images (telescope spiders, stellar halo, etc.), whereas objects like planets, which move due to the rotation between the frames, should not leave a significant residual in the median image. The median can then be subtracted from the individual frames, theoretically only leaving light from those objects and noise. For polarimetry however, rotating the images increases the amount of smearing when using four images with different half waveplate rotations when correcting for instrumental polarization. Therefore, for our purpose the rotation angle between images should be kept small, whereas the search for other objects like planets would work better with a larger rotation angle. Figure 2.6 gives a schematic overview of the entire process for the case of detecting a planet around a star.
For our main data reduction, the ADI technique is not relevant, because we focus on the disk, rather than finding planets. In our case we thus only have to de-rotate the frames.

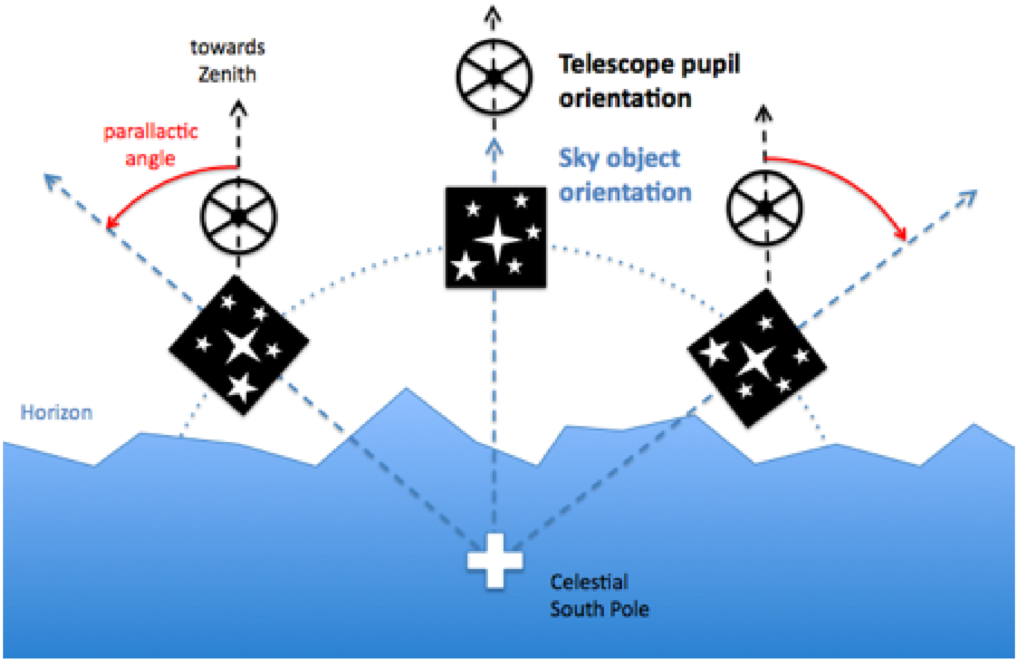

Figure 2.5: Sketch of the field rotation [30]. As the star moves along the sky, the field is rotated with respect to the orientation of the telescope pupil.

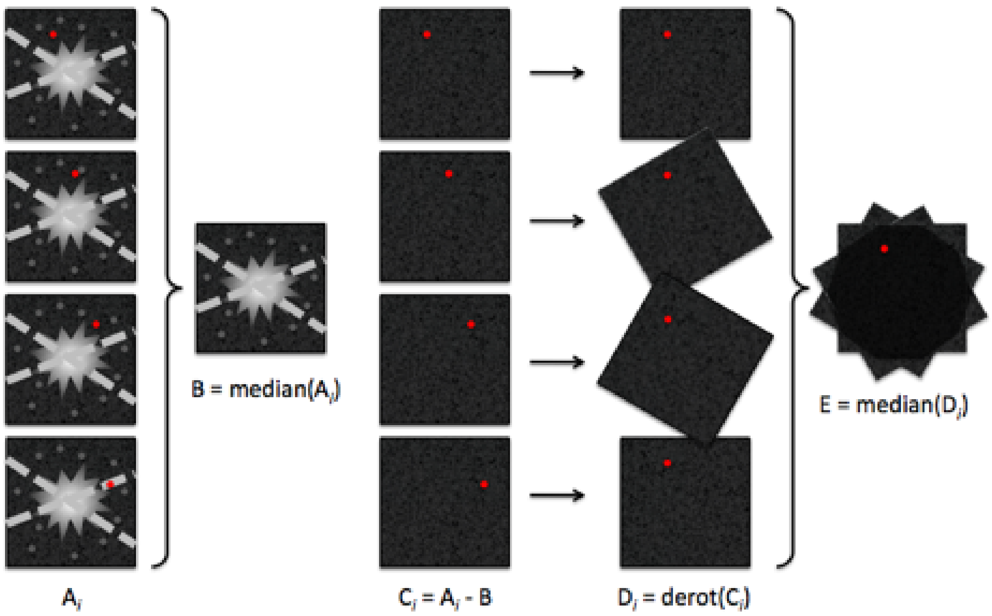

Figure 2.6: Schematic overview of the ADI reduction process [30]. The red dot denotes the position of a planet. The images in A are the ADI rotated frames. These are combined by taking the median into image B, to get the parts which are consistent through the entire observation like the stellar halo and telescope spiders. Image B can then be subtracted from all the images in A, leaving images with only the planet (C) at different rotations. These are then derotated and used further.

Chapter 3

Scattered Light Imaging

The main part of this work involved the processing of our scattered light observations with HiCIAO. Our data was obtained from observations with the Subaru telescope HiCIAO instrument in the sixteenth run of the Strategic Explorations of Exoplanets and Disks with Subaru (SEEDS) survey. The observations took place on the fifth of July 2012 from 20:25 until around 21:30 HST (Hawaiian Standard Time). The images were taken in the H-band (1.6 μm) using HiCIAO's qPDI mode together with ADI mode and no coronographic mask was applied.
The data reduction was a long, complicated process due to several unique characteristics from the instrument and the conditions during the observations. All the details of the steps we went through will be given in the following sections of this chapter. For most of the steps in the data reduction we used tasks from the Image Reduction and Analysis Facility (IRAF) software package. A summary of our data and the conditions of the observations are given in Table 3.1.

(a) Observation conditions and science data

Observation date	05/07/2012
Telescope and mirror size	Subaru, 8.2m
Instrument	HiCIAO
Observation modes	qPDI & ADI
Observed wavelength	H-band (1.6 μm)
Diffraction limit at observed wavelength ($\sim \lambda/D$)	0.05 arcsec
R-band magnitude during observations	11.6
Number of science exposures	68
Exposure time	30 seconds
Image naming	HICIAO00099...
Image numbers	889 to 956
Pixel scale	$9.5 \cdot 10^{-3}$ arcsec

(b) Dark frames and flat fields

Observation date dark frames	07/07/2012
Number of exposures	100
Exposure time	40 seconds
Observation date flat fields	13/05/2012
Number of exposures	9
Exposure time	120 seconds

(c) Photometric standard star data

Standard star name	HD203856
Observation date	05/07/2012
Number of exposures	3
Exposure time	1.5 seconds

Table 3.1: Summary of the observations and the obtained data

3.1 Bad Images

Somewhere along the data reduction process, we noticed that in some of the images the star got fainter and in one case almost completely disappears. We checked this by measuring the Full Width at Half Maximum (FWHM) of the stars in both channel 1 and channel 2 using IRAF's "IMEXAM". Most of the images that looked clean by eye had a value for the FWHM of around 14 pixels with some offshoots to 17.5 pixels. At image HICIAO00099926 however, the value suddenly increases to more than 48 pixels. HICIAO00099929, the image where the star has almost completely disappeared, got an indefinite value in the FWHM measurement. These two images (see Figure 3.1) were therefore removed them from the data set. The cause for the high FWHM will be investigated in the next paragraphs.

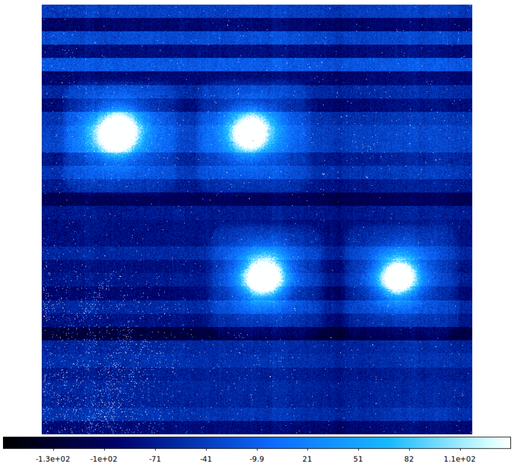

(a) Bad image HICIAO00099926

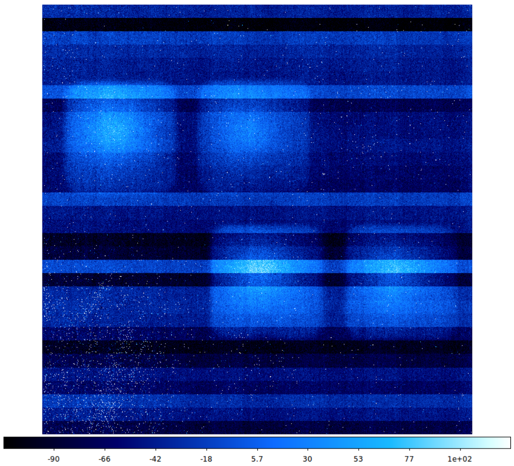

(b) Bad image HICIAO00099929

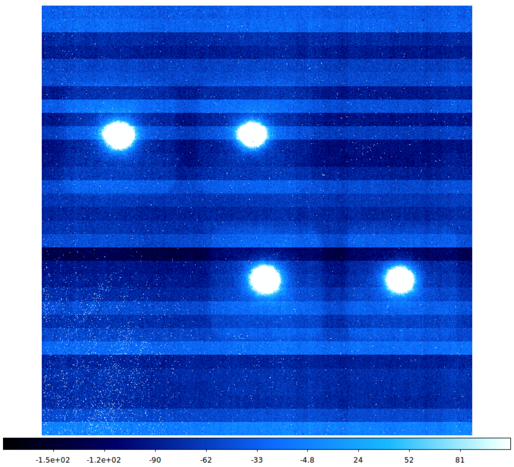

(c) Normal image HICIAO00099889

Figure 3.1: Bad images and an example of a normal one for comparison. For all images, the scales are given in ADU.

Even though there was no mention of problems with the weather in the observation log, it could be that it was still slightly cloudy, causing the decrease in flux in some of the images. To confirm this, we checked the sky attenuation plot given in Figure 3.2. It can be seen that the attenuation during the entire night did not get much higher than 0.1, which should not have given any serious problems.

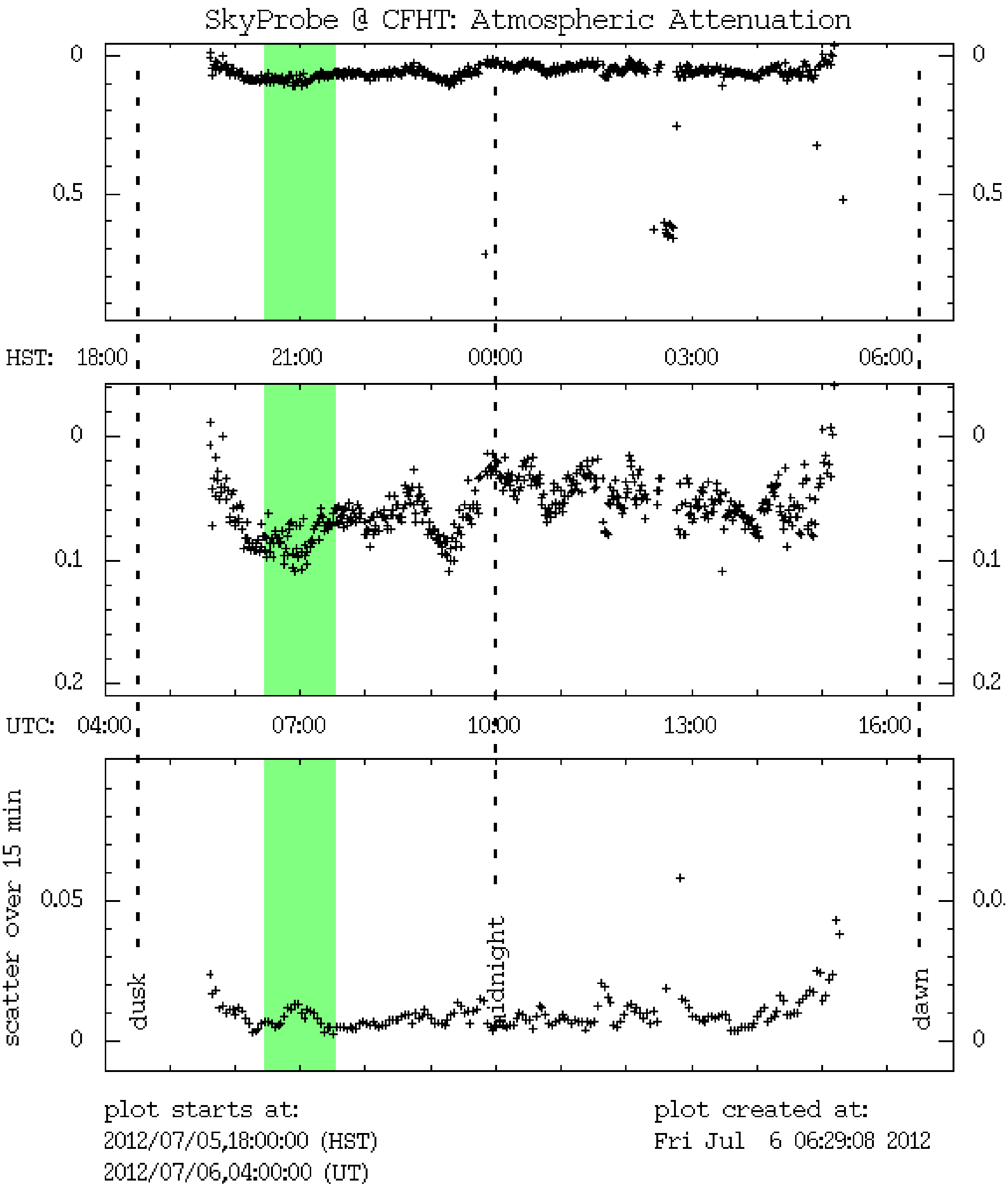

Figure 3.2: Graph of the sky attenuation (or extinction) during the night of the observations [31]. The middle pannel is a zoomed-in version of the upper one, whereas the lower pannel gives the scatter in bins of 15 minutes. The green areas denote our observation window.

We then looked at the natural seeing during the observations. If the seeing is above 1", the Adaptive Optics correction gets worse. Looking at the seeing data for the night of the observations (see Figure 3.3), the seeing was above 1" during the entire period covering our observations. So it seems likely that the natural seeing was too bad to be corrected for by the Adaptive Optics, which could lead to more inaccuracies in the data later on. We will return to this discussion in Section 3.2.8

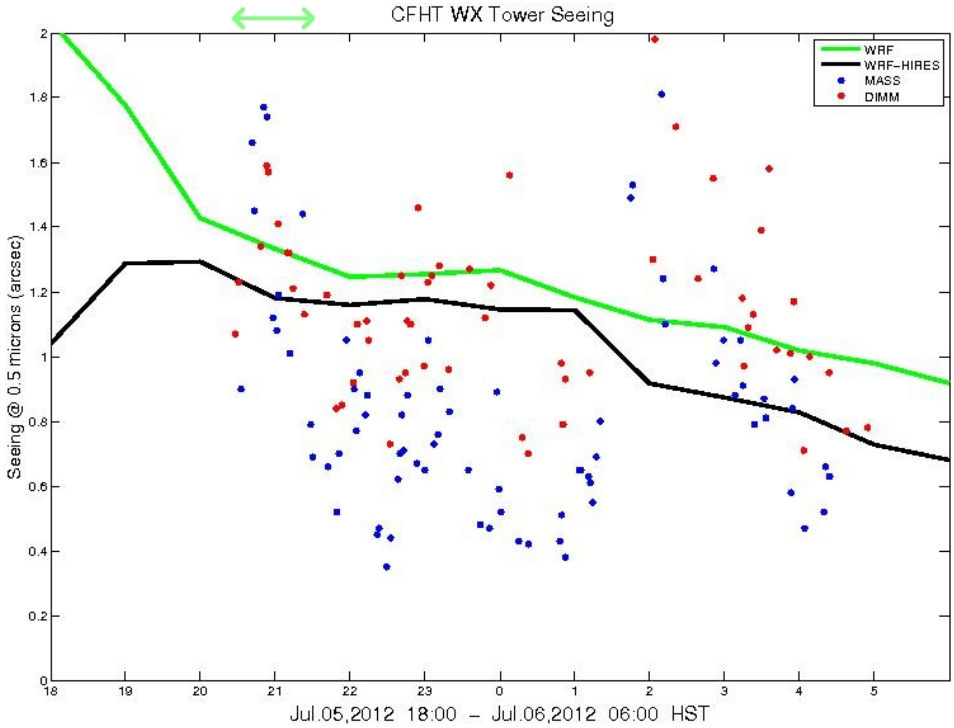

Figure 3.3: Natural seeing during the night of the observations [32]. MASS and DIMM are the names of the software used for the measurement. The two lines drawn give the trends from weather forecast models. The green arrow at the top denotes the observation window.

3.2 Data Reduction Steps

The following sections will explain in detail, the separate steps we performed to reduce the data and get the Stokes parameters.

3.2.1 Destriping

One of the first things that is noticed when viewing the raw data is the presence of both a vertical and horizontal stripe pattern. The horizontal ones each have a width of 64 pixels, whereas the vertical ones are less consistent. It is possibly caused by temperature fluctuations in the detector array and is present in both the science frames and the dark frames. Getting rid of the pattern turned out to be rather difficult. We used a code specifically written for this purpose by Prof. H. Shibai. It starts with a crude (coarse) destriping of all the images to get rid of the horizontal stripes. The code uses a small region at the edges of all the images within the stripes with a width of 4 pixels. These rows of four pixels at the edges are used to store the dark current information. The code takes the average value of that area and subtracts it from every pixel in the stripe. The result of the coarse destriping can be found in Figure 3.4, which still contains both the vertical stripes and remnants of the horizontal ones.

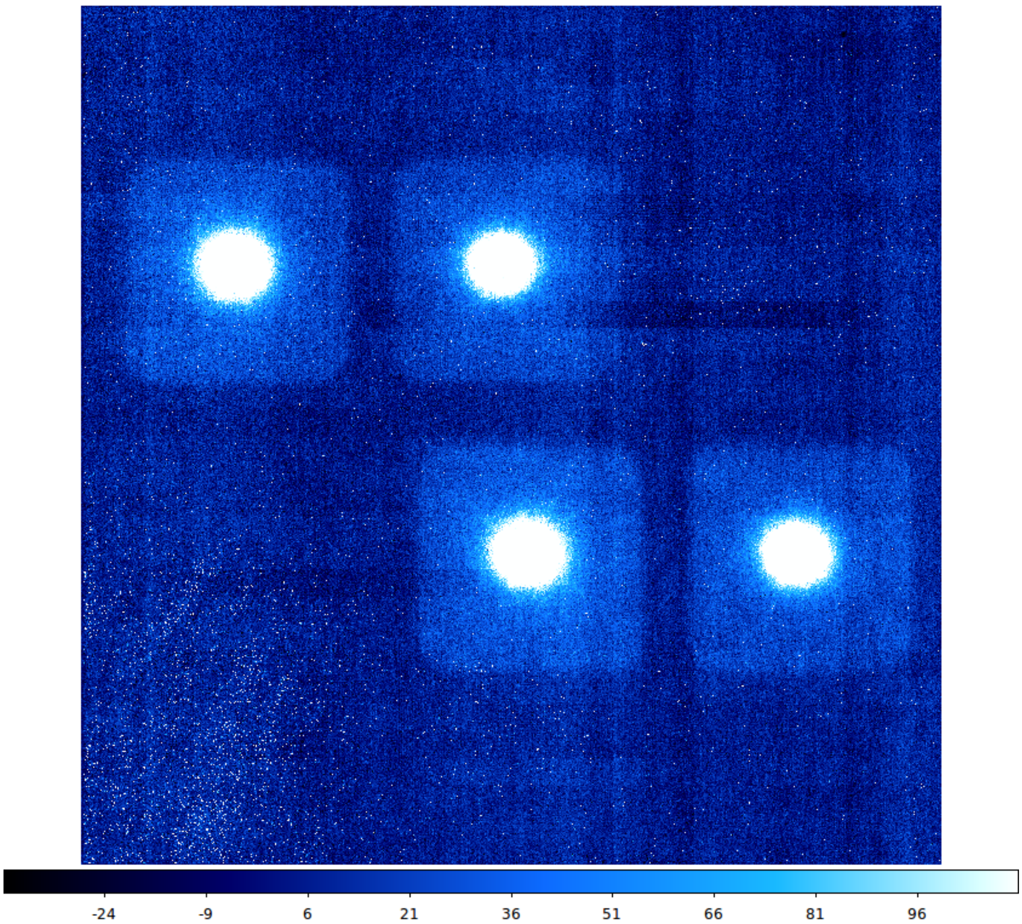

Figure 3.4: Coarse destriped image: HICIAO00099889. A crude removal of the horizontal stripe pattern using the 4-pixel wide edges of the image. The remaining horizontal stripes and the vertical ones still require more steps to be removed. The colorbar is given in ADU.

Next, it creates a mask pattern using the flat frames and the parameters inserted into the code that give the size and location of the qPDI windows and the radius of a circle that encompasses all the light from the star (HALR1, HALX1, HALY1, FRRR1, FRSRL1, FRSRT1, FRSRB1, etc.) to determine which areas in the images are suitable for further analysis of the stripes. Normally the code would use the full PDI windows for the rest of the destriping code and only ignore a circle large enough to block out any light coming from the star itself. In our case however, we used qPDI mode, which has four small windows of only 511 x 511 pixels (white regions in Figure 3.5) and taking out the stellar mask (blue circle within the qPDI within the qPDI windows in Figure 3.5) then leaves only a very small region that can be used.

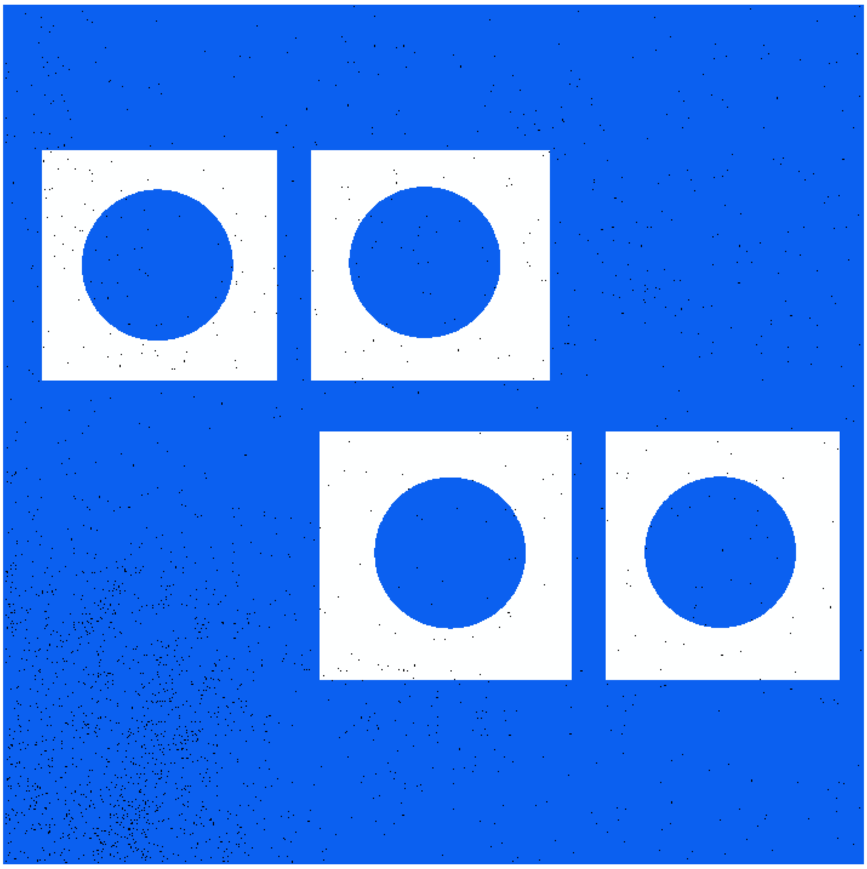

Figure 3.5: The stellar mask. The white regions denote the qPDI windows, with a value of 0 ADU, whereas the circles inside those show the stellar mask. Black pixels have a negative value of -2 ADU and represent bad pixels. Only the blue pixels outside of the qPDI windows were used for determining the stripe pattern. All blue pixels are set to -1 ADU.

Because the stripes are caused by the detector array itself, the stripe pattern should not be different inside the qPDI windows from the area outside these windows. Therefore, we modified the code to instead continue the destriping process using only the areas around the qPDI windows (blue pixels around the white areas in Figure 3.5). In order to remove the rest of the stripe pattern (both vertical and horizontal), the code then divides the horizontal stripes into two groups, corresponding to the alternating pattern. The even and odd numbered stripes are combined into so called "master stripes" to increase the signal to noise level. A stripe pattern is then created by alternating the master stripes, which is subtracted from the images. As a final step , the code then takes the average in every stripe once more and subtracts this from the pixels in the stripe to get the background level to zero counts. Because of this, the code has already performed the normal dark- and sky subtraction processes, but nevertheless, the dark frames are still necessary to remove both hot and so called warm pixels. Furthermore, the pixels outside the qPDI windows are set to a value of -10.000 ADU. The final result of the destriping process is shown in Figure 3.6. A full list of the parameters used can be found in Appendix A and some of the important ones in Table 3.2.

Maximum dark level	1000.0 ADU
Minimum dark level	-800 ADU
Maximum STD dark images	30.0 ADU
Minimum STD dark images	1.0 ADU
Threshold level warm pixels	50.0 ADU

Table 3.2: List of important parameters for the destriping code and their values

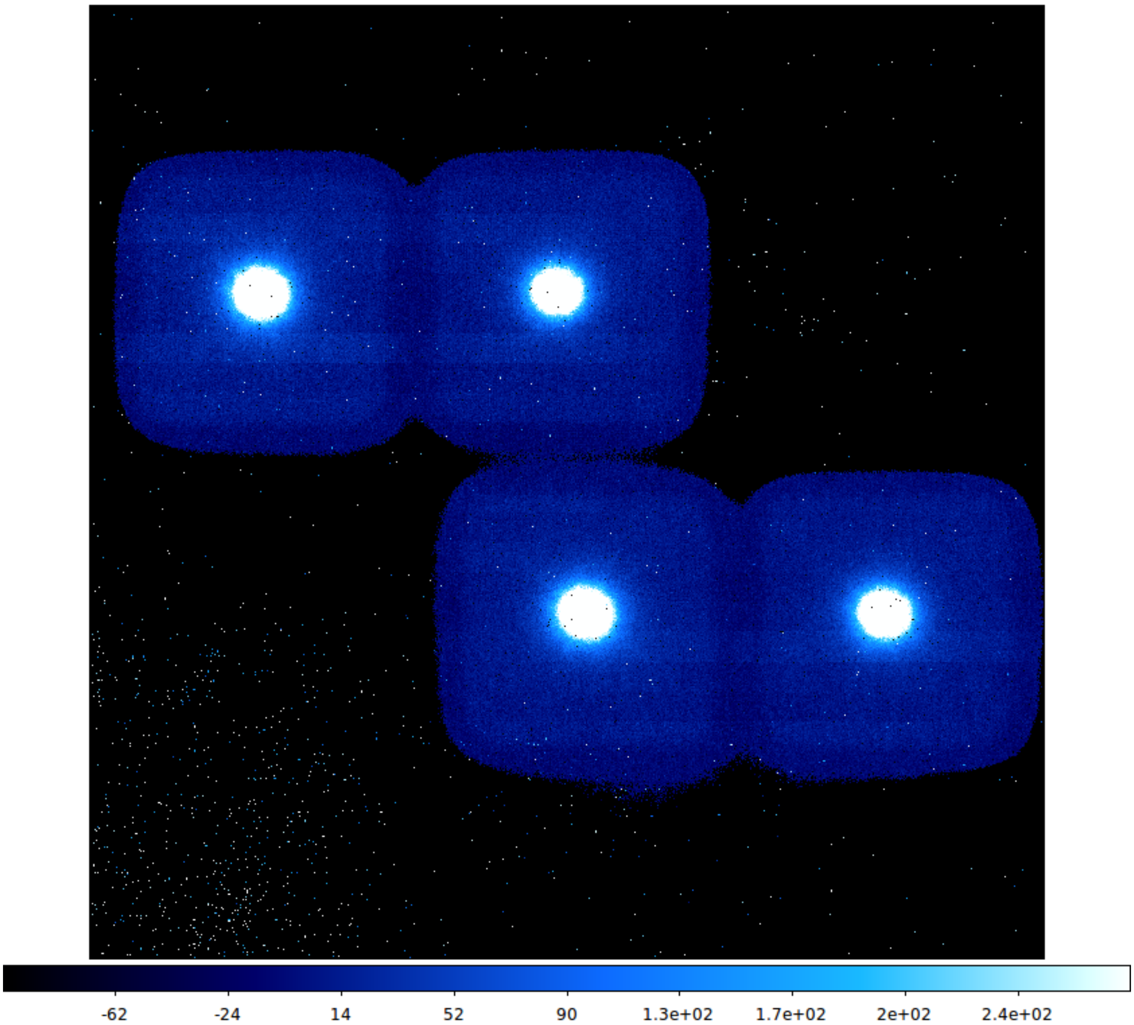

Figure 3.6: Fine destriped image: HICIAO00099889. Here both the horizontal and vertical stripes have been removed as much as possible. Pixels outside the qPDI windows have been set to a value of -10.000 ADU (Black). The colorbar gives the scale in ADU.

3.2.2 Warm Pixel Removal & Flat Fielding

One of the results from the destriping code is an already combined image of the 100 destriped dark frames. This was subtracted from the data to correct for the warm pixels. These are pixels that have too high a value to be reasonable data, but too low to be identified as hot pixels. They usually appear as the four pixels surrounding a hot one (See Figure 3.7).

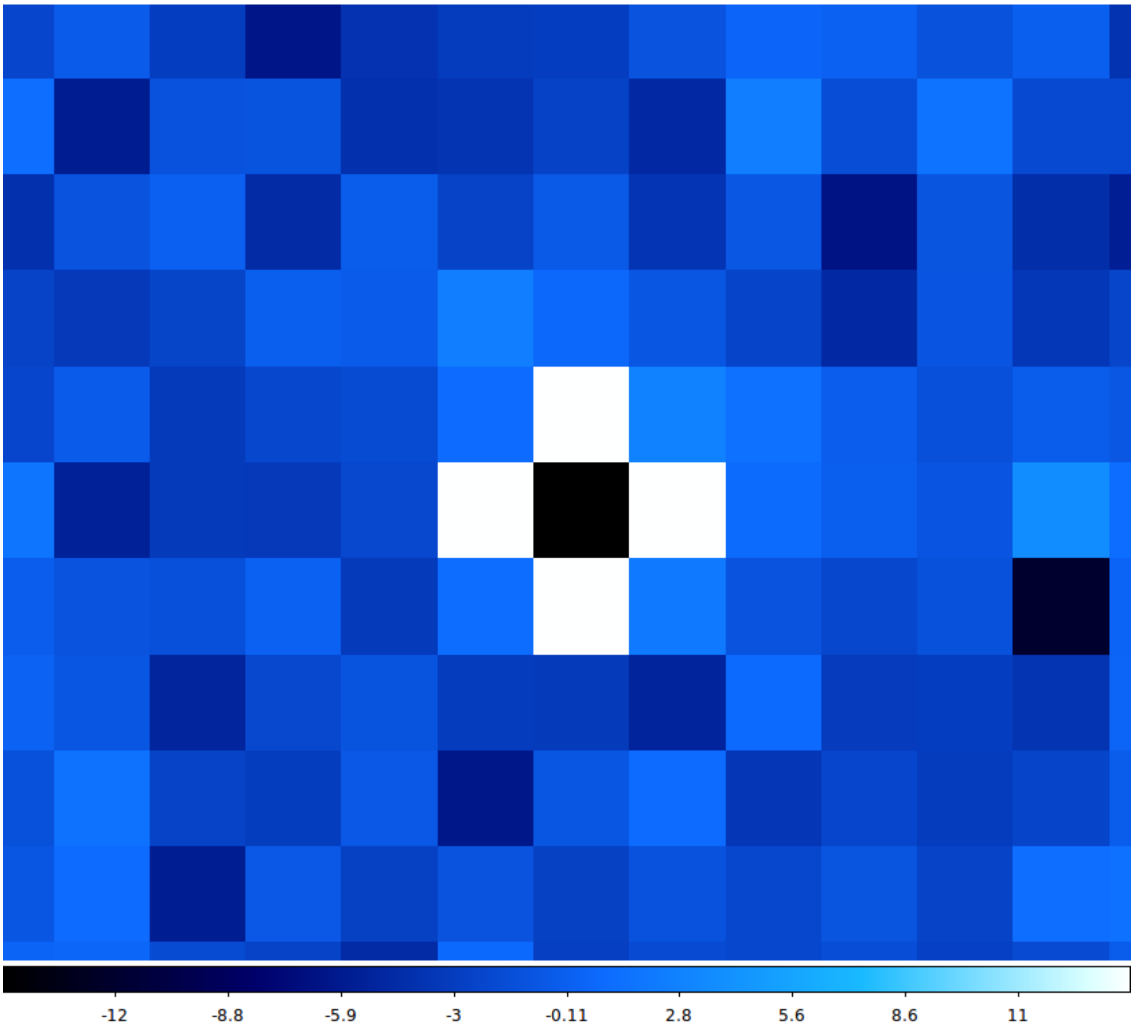

Figure 3.7: Example of warm pixels (white) around a hot pixel (black) in the combined fine destriped dark image. Again, the color scale is given ADU.

Looking at the combined dark frames, there was an apparent transition in pixel values present halfway through the image (see Figure 3.8). Using "IMSTAT" with 10 sigma-clipping iterations and both an upper and lower clipping factor of 5.0, we determined the background level on both sides. The left side has a median background value of 0.5169 ADU with a standard deviation of 2.17 ADU and the right side was found to be -1.673 ADU with a standard deviation of 2.114 ADU. Although the systematic difference can be seen between the left and right, because the standard deviation is almost as large as the difference between the averages, it should not be a significant difference. The next paragraphs describe a number of possible causes that we investigated.

The pattern could not be found in any of the individual fine destriped dark frames, probably due to a too low signal-to-noise ratio. In order to check if something might have gone wrong with the combination of the images, we also manually combined them using the IRAF task "IMCOMBINE". This gave exactly the same result as the destriping code and thus the separation in the image appears to be real. A possible explanation could be that the unmasked region in the center of the images (see Figure 3.5) used by the destriping code to determine the verticle stripe pattern is a lot smaller in between channel 2 and 3 than in other areas of the image, making it harder to get a good estimate of the stripe pattern there. The pixel count level of that incompletely removed stripe then remains in the rest of the image.

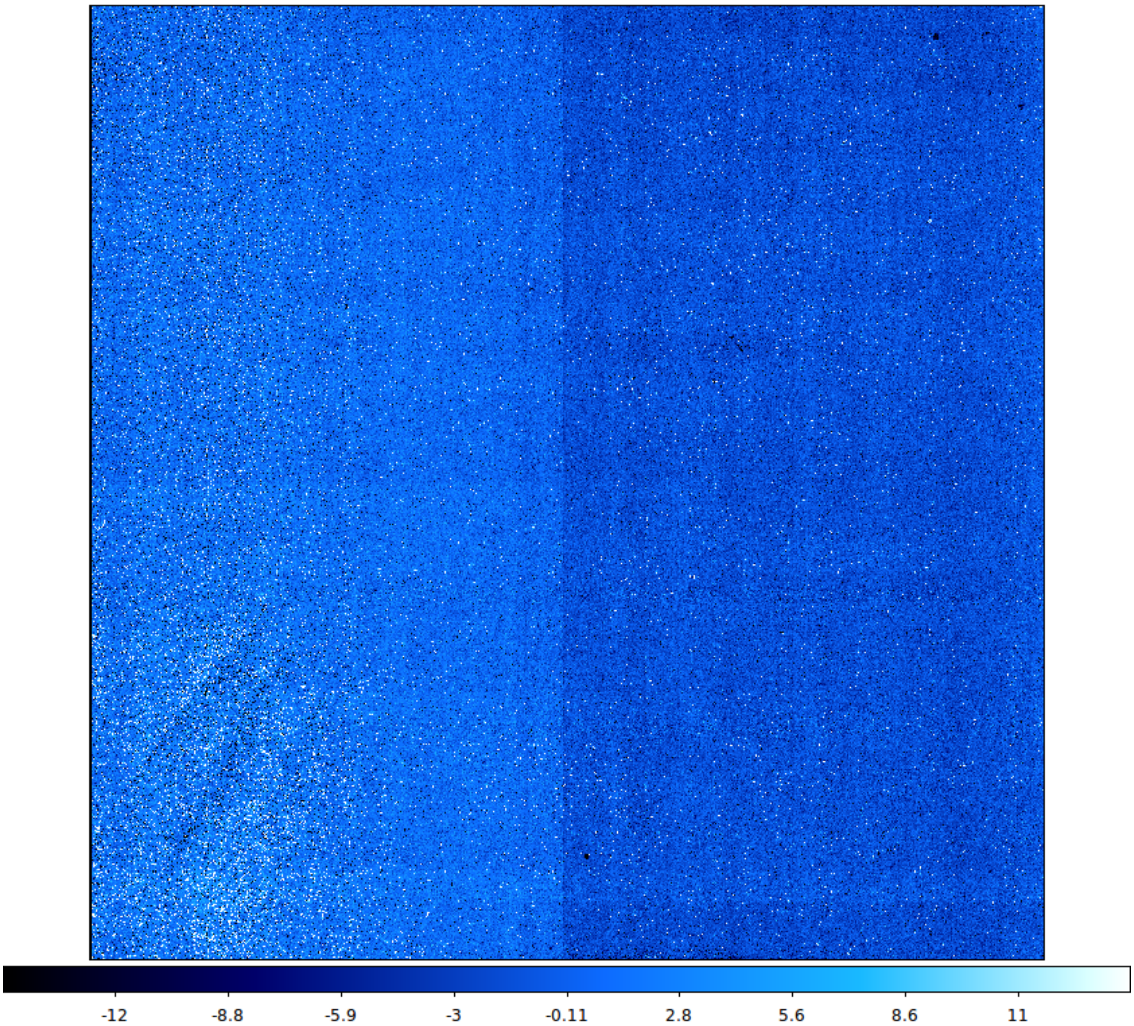

Figure 3.8: The combined image of the 100 fine destriped dark frames. The color scale is shown in ADU. The image has a clear separation in the middle. On the left side the median background value equals 0.5169 ADU with a 2.17 ADU standard deviation. The right side has a median value of -1.673 ADU with a standard deviation of 2.114 ADU.

Another problem was that the dark frames were obtained with a longer integration time than the science data, because there were no recent frames available with the same integration time. Therefore we had to multiply the combined dark frame image with a correction factor before subtracting it from the science data. In an ideal case this number would be the ratio of the two integration times, but the dark level does not necessarily have to scale linearly with time. Due to the imperfect destriping process, too high a correction factor would actually introduce the same pattern found in the combined dark frame, into the science data. We tried several values to see what would remove the warm pixels the best and found that a value of 30s/40s did give the best results, showing no significant sky level in the images after the distortion correction (Section 3.2.4).
After the dark subtraction, the flat frames were combined using "IMCOMBINE". Together with 3-sigma clipping, we used the median of the images to prevent hot pixels that were not removed yet from affecting the average. Next, the combined frame was normalized by dividing it by its mean with "IMARITH". The flat field correction was then performed on the science frames by dividing all of them with the normalized flat field image.

3.2.3 Bad Pixel Correction

Correction for the bad pixels in the image was performed in three stages. We started with applying "FIXPIX", which uses a bi-linear interpolation to replace the bad pixels. In order to locate them, it needs a bad pixel map, for which we used the one that was created by the destriping code.

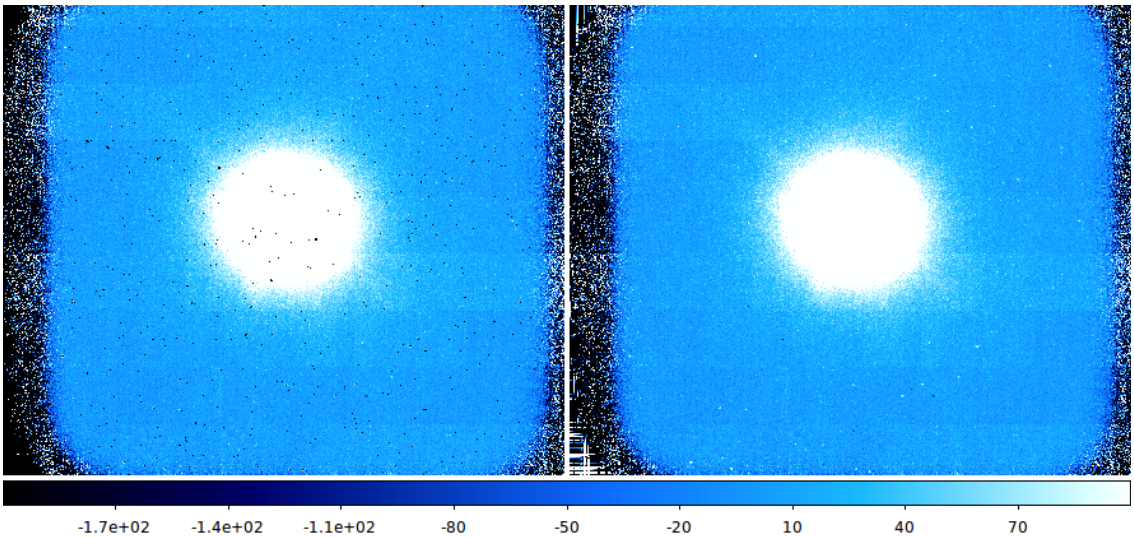

Figure 3.9: FIXPIX result on HICIAO00099889. The colorbar denotes pixel values in ADU. Left is before and right is after using Fixpix.

After running "FIXPIX", there were still some hot pixels left in the data (see Figure 3.9). Therefore, another bad pixel correction was performed using the IRAF task "COSMICRAYS". Here a pixel is considered to be a cosmic ray hit or a hot pixel if its value is significantly higher than the mean value of the four surrounding pixels. The threshold for such a bad pixel was set on a value of 15. "COSMICRAYS" then interpolates the correct value by taking the average of the four pixels around it. We also attempted to remove bad pixels still present with negative values. This was done by first inverting the images (multiplying with -1) using "IMARITH" and then running "COSMICRAYS" again with the same parameters, before re-inverting the images.
In order to furher improve the bad pixel correction we redid the "FIXPIX" correction but now

using a bad pixel mask that is created from the combined dark image. Here we took all pixels with a value above 50 ADU and all those below -100 ADU and replaced them with a value of 10000. All pixels with a value between -100 ADU and 50 ADU (the good pixels) were replaced by a value of 0. This is a more aggressive correction, but it managed to further remove some of the bad pixels still present in the images.

3.2.4 Distortion Correction

Due to slight distortion created by the optics, each pixel does not necessarily represent the same size of 9.5 mas (milli-arcsecond) on the sky. This can be corrected, but it requires detailed knowledge of its effect. First the images were divided into their four separate channels using "IMCOPY".

$$imcopy \quad image[x1:x2, y1:y2] \quad channelname$$

Each channel could then be corrected for distortion using the task "GEOTRAN", which uses a coordinate transformation for the correction. It requires the input of two files, one that gives the coordinate transformation itself and the other listing the locations within the first file to find the correct coordinates for doing the transformation. Both files were provided by the SEEDS project, where the distortion was measured using observations of the globular cluster M15.

3.2.5 Position Matching & Stokes Parameters

Once all the previously described steps have been excecuted, the Stokes parameters can be obtained by making different combinations of the channels. Stokes I is acquired by adding the two orthogonal polarization states. The others can be found using equations (1.6) and (1.7), which come down to a simple subtraction of channel 2 from channel 1 (or channel 4 from channel 3 for the lower channels). Whether the resulting image equals either Q or U depends on the rotation angle of the half waveplate for that particular frame. Using the polarization angle conventions in the upper channels as given in Section 1.4.1, Stokes Q and U are obtained as the following:

$$I_{ch1}^{0^\circ} - I_{ch2}^{0^\circ} = +Q \tag{3.1}$$
$$I_{ch1}^{45^\circ} - I_{ch2}^{45^\circ} = -Q \tag{3.2}$$
$$I_{ch1}^{22.5^\circ} - I_{ch2}^{22.5^\circ} = +U \tag{3.3}$$
$$I_{ch1}^{67.5^\circ} - I_{ch2}^{67.5^\circ} = -U \tag{3.4}$$

The superscript angles denote the rotation angle of the half waveplate. Fully applying the technique described in Section 2.2.1, the speckle noise corrected Stokes Q can then be obtained by subtracting the -Q image from the +Q one and the same holds for Stokes U.

$$Q = \frac{+Q - (-Q)}{2} \tag{3.5}$$
$$U = \frac{+U - (-U)}{2} \tag{3.6}$$

Before subtracting the individual channels from each other however, it is first necessary to match the position of the star within each image. The IRAF task "CENTER" was used for this purpose. It requires the input of an initial guess for the center of the star. Between individual images, the star did not seem to jump in position very drastically, so for the initial estimate, the center of the star in just one of the images was determined using "IMEXAM". Other parameters that need to be set are the FWHM of the point spread function (PSF) of the star (14 pixels was used, as was determined in Section 3.1), the algorithm with which to find the center (centroid in this case) and the width of the box within which to find the real center, which was set to 10 pixels. Using the resulting center coordinates from "CENTER", the stars were then all shifted to a common position at coordinates [X:261,Y:327] with the task "IMSHIFT".

3.2.6 Instrumental Polarization

Light from the source does not directly fall onto the CCD, but instead goes past a set of optical elements (mirrors, half waveplate, image rotator, prisms, etc.). With each interaction, the light obtains an extra amount of polarization. This is an inherent property of the telescope and the instrument that needs to be corrected for. The Stokes images we get from observations (Q' or U', depending on the half waveplate angle) can be described as a linear combination of the real Stokes parameters:

$$I_{left} + I_{right} = x_{11}I + x_{12}Q + x_{13}U = I' \tag{3.7}$$

$$I_{left} - I_{right} = x_{21}I + x_{22}Q + x_{23}U = Q' \,\mathrm{or}\, U' \tag{3.8}$$

Here x_{nm} are constant numbers giving the fractions of the real Stokes parameters "hidden" in the observed Stokes parameter. Subtracting this for a half waveplate angle of 45 degrees from the one with an angle of 0 degrees or 67.5 degrees from 22.5 degrees then gives the following set of equations.

$$Q' - (-Q') = 2Q' = \left(x_{21}^{0} - x_{21}^{45}\right) I + \left(x_{22}^{0} - x_{22}^{45}\right) Q + \left(x_{23}^{0} - x_{23}^{45}\right) U \tag{3.9}$$

$$U' - (-U') = 2U' = \left(x_{21}^{22.5} - x_{21}^{67.5}\right) I + \left(x_{22}^{22.5} - x_{22}^{67.5}\right) Q + \left(x_{23}^{22.5} - x_{23}^{67.5}\right) U \tag{3.10}$$

Here the superscript number above the coefficients denotes the angle of the half waveplate. For Stokes I, the non-polarized component is the dominant component. Therefore, the coefficient x_{11} should be much larger than x_{12} and x_{13}. The corresponding equation for Stokes I then becomes:

$$I' = \langle x_{11} \rangle I = \frac{\left(x_{11}^{0} + x_{11}^{45} + x_{11}^{22.5} + x_{11}^{67.5}\right) I}{4} \tag{3.11}$$

This completes a set of three equations (3.9, 3.10 and 3.11) with three unknowns (Q, U and I), which can be solved for the real Stokes Q and U through a simple matrix equation. The coefficients themselves need to be determined first based on all the different components in the telescope and instrument. We used a method described by Hashimoto et al. [33]. This involves taking the reflection and refraction of the light by each of the mirrors in the telescope into account using the Fresnel equations and using these to get a set of equations for the coefficients x_{nm}. Our values for x_{11} were larger than x_{12} and x_{13} by at least two orders of magnitude, justifying the use of Equation 3.11. In order to perform the entire instrumental polarization calculation, a full set of polarization states is required. The consequence of this is that if one of the images needs to be removed, the other three images in its cycle also become useless.

3.2.7 ADI De-rotation

Now that the Stokes Q,U and I images have been corrected for instrumental polarization, the next step is to derotate the images taken in ADI mode. The rotation angle of each image can be calculated using the information provided in the header (position of the object, time of the observation, telescope location, etc.) as was mentioned in Section 2.2.1. The rotation angle was obtained for every observed image and the Q and U images were made using combinations of two of these images. ADI correction therefore requires de-rotating the Q and U images with an average of the two angles.

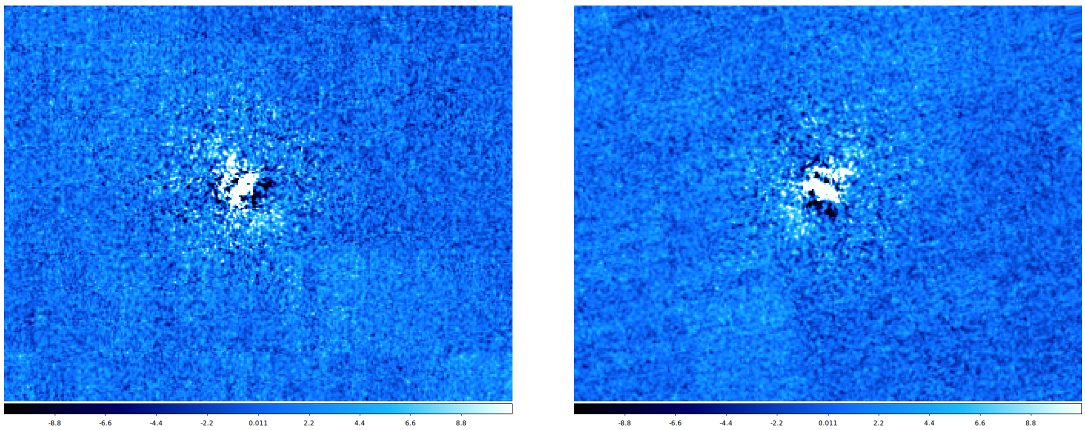

(a) Before (b) After

Figure 3.10: ADI de-rotation effect of one of the Stokes parameter images. The color scale is given in ADU.

Using these angles, the Stokes parameter images can then be de-rotated using the IRAF task "ROTATE", the effect of which is shown in Figure 3.10. The angle used in "ROTATE" is the calculated rotation angle together with the offset angle which can be found in the fits-file header under the parameter 'D_IMRPAP' (122.171 for our data).

Averaging Stokes Q and Stokes U over the waveplate cycles, the final Stokes parameters are given in Figure 3.11, where we have still kept the two data sets coming from the upper and lower channels separate to check for consistency. For the final results in Section 3.4 we will average over the two. After going through all these steps, the Stokes parameters are ready for use in calculating the polarized intensity (Equation 1.8) and the polarization angle (Equation 1.9), but some considerations still need to be made with respect to the varying image quality already touched upon in Section 3.1.

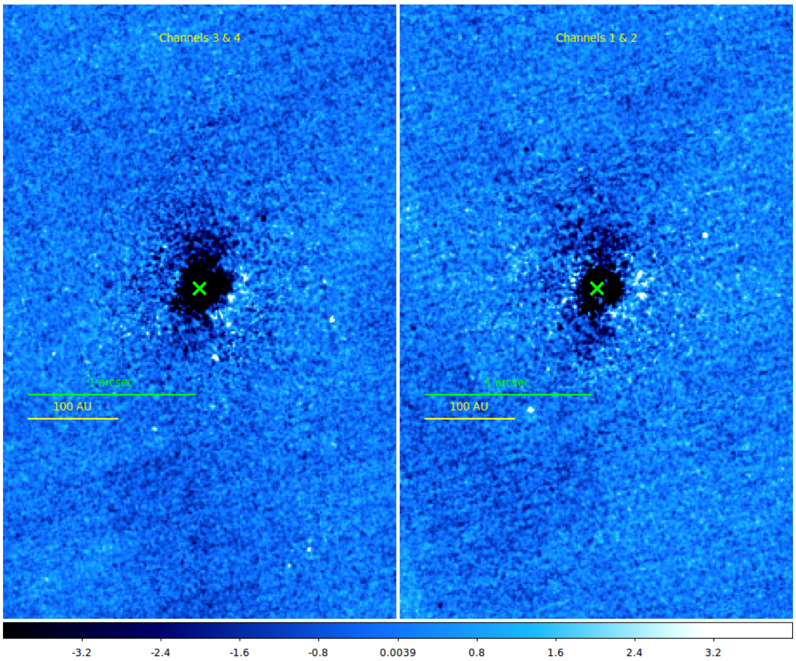

(a) Stokes Q

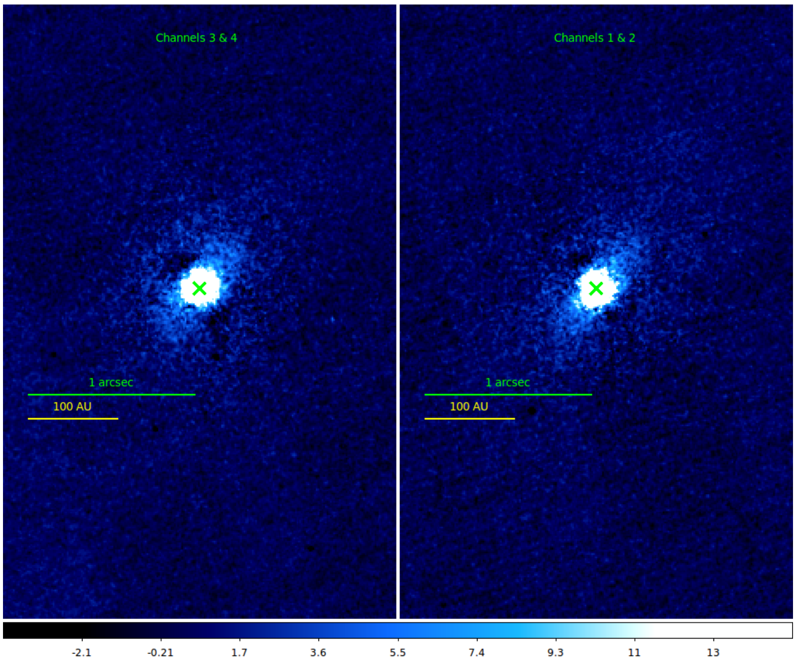

(b) Stokes U

Figure 3.11: Averaged Stokes Q and Stokes U images. The colorscale gives pixel values in ADU and the green cross denotes the stellar position. We have kept the two data sets separate here from the upper and lower channels to check for consistency.

3.2.8 Another Look at Bad Images

The smallest separation that we can discuss is called the inner working angle and it depends first of all on the diffraction limit of the telescope, but is further increased due to smearing effects from the point spread function and other sources of noise. Therefore, it is desirable to have an FWHM of the PSF which is as small as possible and also have as little variation between combined images as possible. As we have already discussed in Section 3.1, there were some problems with bad images and some variation the FWHM of the PSF between images and we already exluded two of the images. Figure 3.12 displays the variation in the FWHM between the remaining images after distortion correction and for every qPDI channel separately.

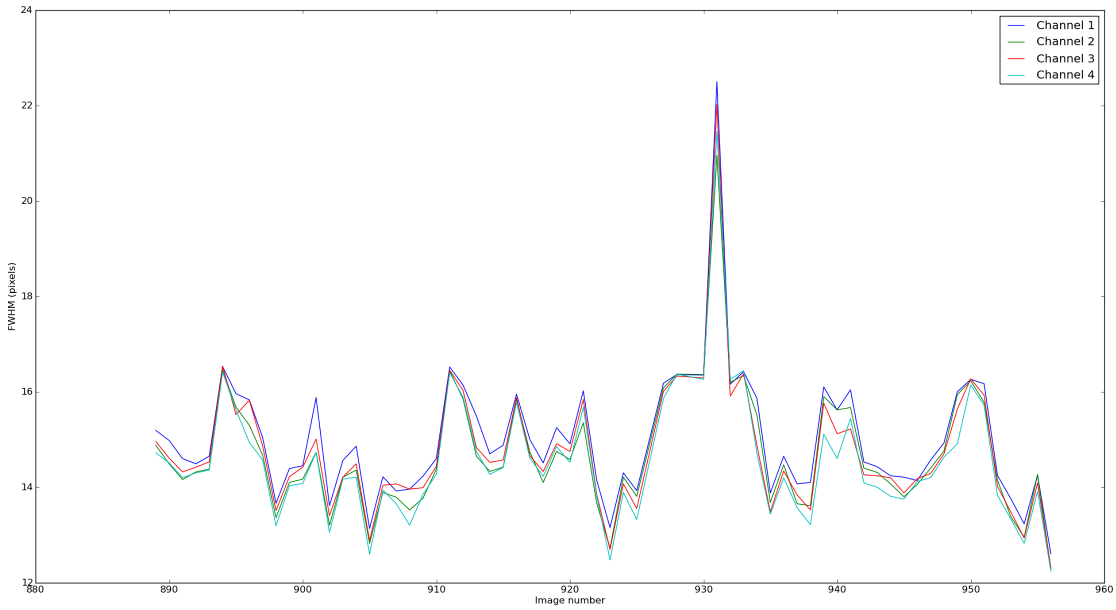

Figure 3.12: FWHM measurements of the images after distortion correction. The different lines give the values for the different qPDI channels.

It shows that there is consistency between the PSF size in the four qPDI channels, but also a lot of variation between the images with one more extreme outlier. In order to perform the IP correction, all four images within a waveplate cycle are required (see section 3.2.6) and thus this outlier was already not taken into account. Even between the other images there is still a variation from 13 to 16 pixels in the FWHM. Therefore, in order to decrease the error in the PI images, we considered removing more of the images, but this does reduce the signal-to-noise ratio. We made the decision to remove all waveplate cycles in which there are images with a PSF FWHM larger than 16 pixels, effectively removing almost half of the data.

3.3 Photometry

All the units in the data so far have been in pixel counts (ADU), which still need to be converted to real fluxes through photometric calibration. The steps taken will briefly be described here. For the calibration, we used photometric standard star data of HD203856 taken in the open use program on July 5th 2012. We first reduced these images in exactly the same way as the science data until the distortion correction step as was described in Sections 3.2.1 through 3.2.4. We then created a Stokes I image by averaging over the Stokes I obtained from the upper and lower channels. This image is then divided by the IP correction factor x_{11} (see Section 3.2.6). These are all the steps required for the reduction before aperture photometry.
The photometry itself was performed using the "PHOT" task in IRAF. This determines the flux at different annuli around the central position and also converts it to a magnitude using the zmag parameter. When the total magnitude value no longer deviates much between annuli, we use that annulus and take the mean magnitude between the different images. This is shown in Figure 3.13. The important parameters are given in Table 3.3. Comparing the measured magnitude of HD203856 to the one from the literature (6.887 [34]) then gives a correction factor for the magnitude. In our case

$$\begin{aligned} m_{real} &= m_{measured} + \Delta \\ \Delta &= -2.560 \pm 0.018 \end{aligned} \tag{3.12}$$

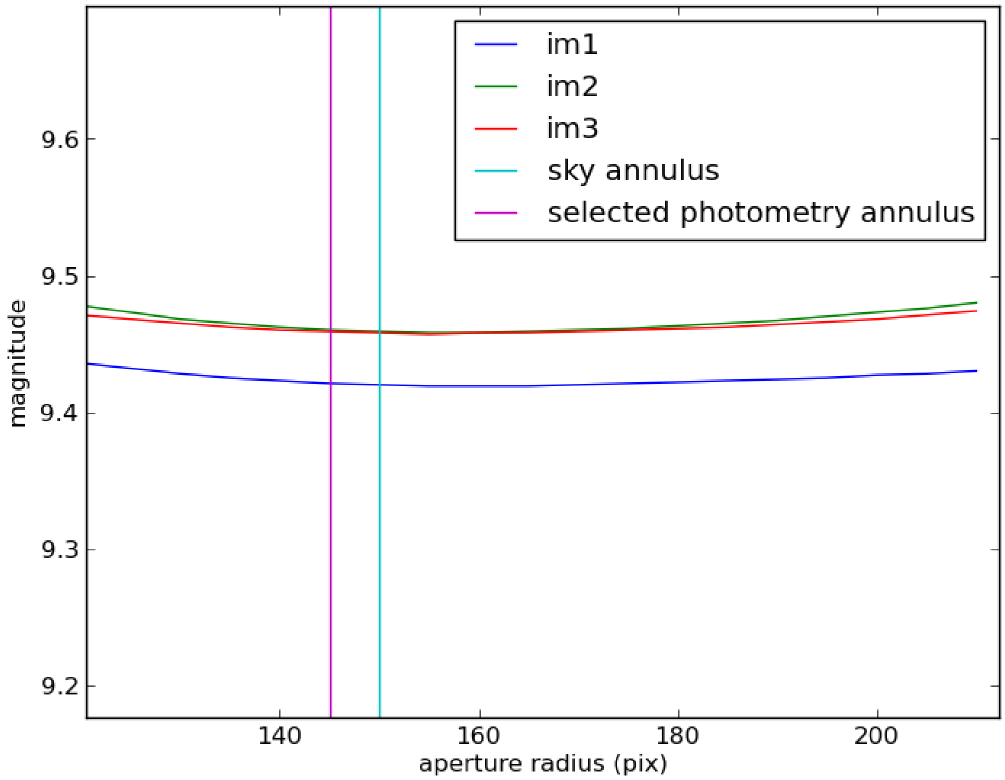

Figure 3.13: Aperture photometry for the photometric standard star HD203856 data.

Because stars are point sources and the intensity stays constant, the number of ADUs giving the corrected magnitude can then be used to determine the conversion factor for the surface brightness of a single pixel. The magnitude can then be converted into a flux using the zero-magnitude flux (F_0, 1050 Jy for the H-band [35]):

$$F = F_0 \cdot 10^{-\frac{m}{2.5}} \tag{3.13}$$

Taking the angular size of a single pixel (9.5 mas by 9.5 mas) into account then gives the conversion factor:

$$1\ ADU/s/pixel = 0.775\ mJy/arcsec^2 \tag{3.14}$$

Parameter	Value	Description
fwhmpsf	14	Rough estimate of the FWHM
readnoi	15	Read-out noise
epadu	1.6	Gain
itime	1.5	Integration time
annulus	150	Inner radius of the sky region
dannulus	15	Radial width of the sky region
zmag	25.0	Zero-point magnitude

Table 3.3: Important parameters used in the "PHOT" task for the photometric standard star.

3.4 Results from the Data

The resulting polarized intensity image, determined through Equation 1.8, is shown in Figure 3.14a, which gives the linearly polarized light coming from the disk. It clearly shows the elongated disk emission, but in the central regions there is a large component of unsubtracted stellar light and noise present. There are also still some speckles present in the image, which could be due to bad pixels not removed properly and then being amplified due to the instrumental polarization correction. In order to get a grasp on the extent of the inner working angle, mentioned in Section 3.2.8, we looked at the signal-to-noise ratio in the image. The error in the polarized intensity was calculated using standard error propagation:

$$\sigma_{PI}^2 = \left(\frac{Q}{PI}\sigma_Q\right)^2 + \left(\frac{U}{PI}\sigma_U\right)^2 \tag{3.15}$$

The errors in the Stokes parameters, σ_Q and σ_U, were determined by taking the standard deviation over all the waveplate cycles used to get the average Q or U image and dividing by the square-root of the number of cycles. We then divided the PI images by the error images using IMARITH to get to get the 'Signal to noise' (SNR) map shown in Figure 3.14b. Because the stellar light dominates in the central region, we took the radius at which the mean SNR drops below 3 as the region where the disk emission is separated clearly enough from the noisy center. This then gives an inner working angle of 133 mas, or 24 AU.

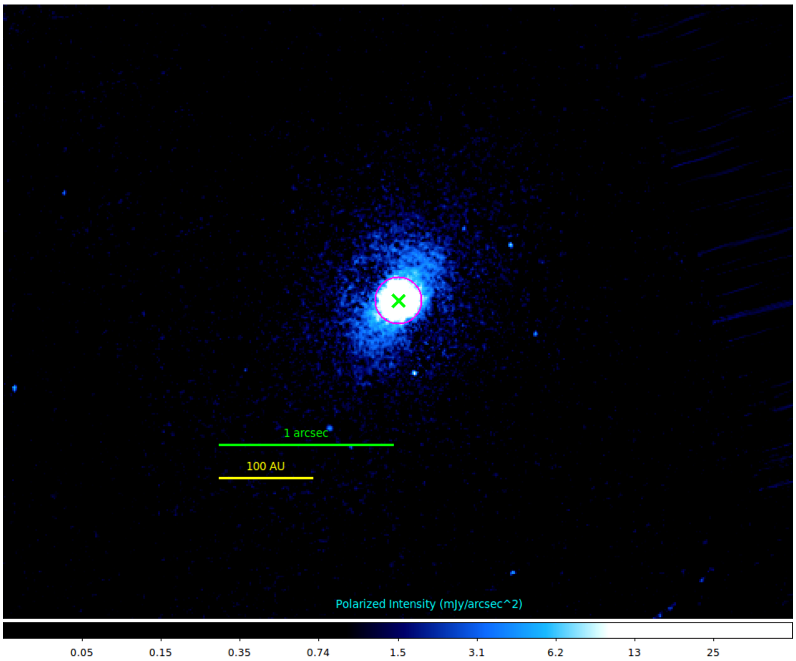

(a) Polarized Intensity with units for the colorbar in $mJy/arcsec^2$. The magenta circle denotes the inner working angle.

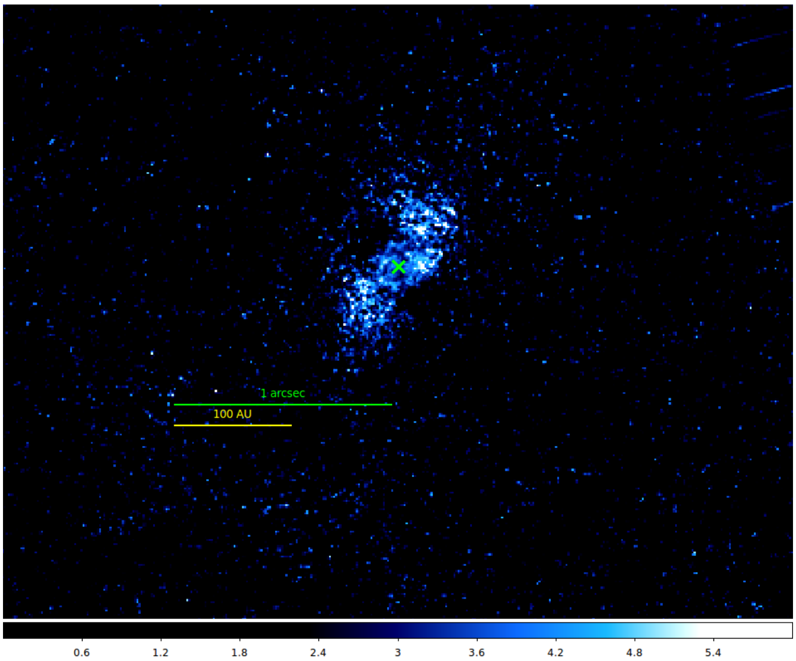

(b) Signal-to-Noise map. The colorbar denotes the SNR.

Figure 3.14: Polarized intensity and signal-to-noise maps. In both images the green cross represents the stellar position.

To confirm that the emission in Figure 3.14a is in fact scattered light from the disk, we can look at the direction of the polarization vector. Calculated using the definition in Equation 1.9, Figure 3.15 shows the polarization angle through the yellow ticks, overlayed on a block averaged version of Figure 3.14a. In the disk region, all the ticks are aligned in a direction perpendicular to the direction towards the stellar position. This is a clear sign that it is indeed light scattered through the disk by the mechanism described in Section 1.4.

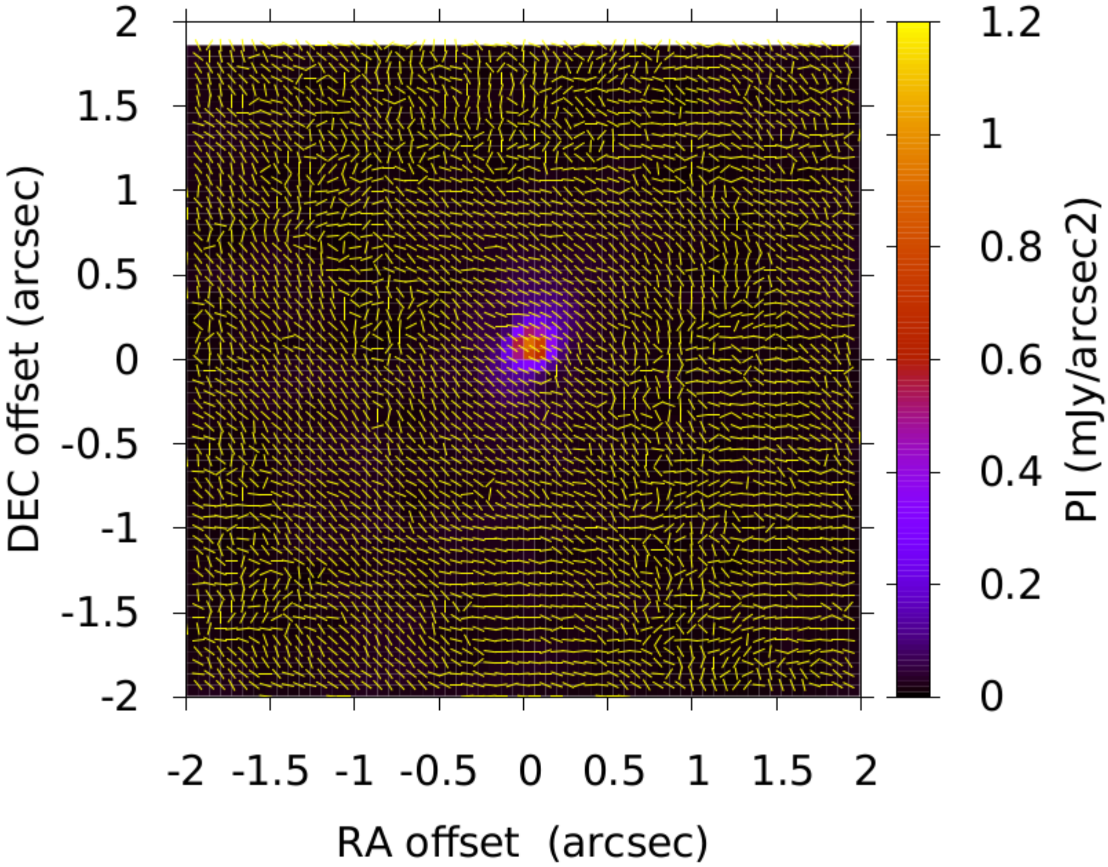

Figure 3.15: Polarization angle map overlayed on a block averaged version of PI. The yellow ticks give the polarization angle. The code used to produce this image was written by Yayoi Maruta.

3.4.1 Physical Parameters from PI

From the PI image, there are a couple of parameters we can determine for the disk. These include the disk outer radius, the position angle on the sky and an estimate of the inclination angle. For the latter two, we used the IRAF task "ELLIPS" to fit an ellipsoid to the image. This then directly gives the position angle of the major axis (PA), measured clockwise from the North, and the ellipticity. The axial ratio (b/a) follows from the ellipticity (e) and the inclination angle (i) can then be calculated with:

$$e \equiv \sqrt{1 - \left(\frac{b}{a}\right)^2} \tag{3.16}$$

$$i = \cos^{-1}\left(\frac{b}{a}\right) \tag{3.17}$$

These relations do assume the disk is infinitely flat, which is not realistic, so it is only an estimate for the true inclination. The disk outer radius (R_{out}) was determined by taking the distance from the stellar position along the position angle at which the SNR drops below a value of 2. The measured disk parameters are summarized in Table 3.4.1 with 1-σ errors.

Parameter (unit)	Value
PA (degrees)	33.9 ± 1.2
i (degrees)	31.74 ± 0.02
R_{out} (AU)	92 ± 12

Table 3.4: Measured disk parameters. The position angle is the angle measured clockwise from North

3.5 Discussion

Taking a look at the observed H-band polarized intensity of RX1615, we clearly see a detection of an extended disk, confirmed by the SNR map and the orientation of the polarization angle (Figures 3.14 and 3.15). Based on the result shown in Figure 3.14a, the scattered light of RXJ1615 does not show any clear structure, such as spiral arms (seen for example in the protoplanetary disk HD142527 [13]) or clumps. However, the low SNR of the image could potentially hide any structure in the noise. We also do not see a clear decrease in emission in the inner region. This seems to contradict the submm visibility map from Andrews et al. [23], but our inner working angle of 24 AU is close to the 30 AU cavity radius. If our inner working angle has been underestimated, the cavity might still fall within it. However, if the results are conclusive, our PI image could point to the possibility of a different distribution for the small dust grains compared to the large ones. In the transitional disk SAO 206462, a cavity has been resolved in both near-IR and submm observations, showing a smaller cavity size for the small dust grains [36], which could also be the case for RXJ1615. Garufi et al. [36] showed that this could potentially be attributed to interactions with a companion in orbit of the star at the smaller cavity radius, creating a pressure bump that pushes the larger dust grains outward.

In Section 1.4.1 we introduced the possibility of using the degree of polarization of the disk to derive properties of the dust content. In order to get the degree of polarization we would have to determine the total intensity of the disk emission. Obtaining this is difficult, because the disk light is completely outshined by the stellar light and removing that accurately requires a very detailed reconstruction of the stellar PSF that can be subtracted from Stokes I, or observations with a coronographic mask. Our data was observed without a coronographic mask and we also do not possess data of a reference star observed on the same night and located nearby RXJ1615 that could be used for determining the PSF.

3.5.1 Giving ADI a Chance

A crude method of removing the stellar PDF is ADI (see Section 2.2.1). Although the rotation angle is small, our data was observed in ADI mode. Therefore, we also performed the corresponding data reduction. We started from the distortion corrected, position matched images, subtracting the median and then derotating all of them. After that, the ADI data reduction follows the same steps as before (see Chapter 3), until we obtain an instrumental polarization corrected Stokes I image. The result is shown in Figure 3.16a. Due to the small rotation angle of our observations, there is a substantial amount of self subtraction, causing Stokes I to become negative in some regions. This makes it impossible to extract the total intensity of the disk. We also do not see any clear sign of a planet in this image, but it would have to be orbiting at a distance distance outside the noisy area of the image in Figure 3.16a for it to be seen. Due to planets being faint objects, the SNR of Stokes I can be more sensitive to a detection, but we cannot distinguish any object in there either (see Figure 3.16b).

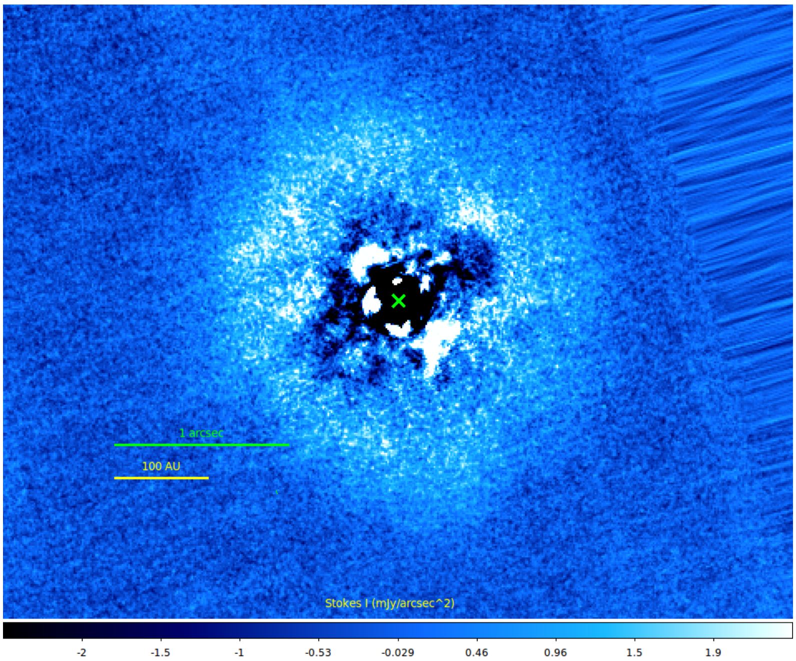

(a) Stokes I

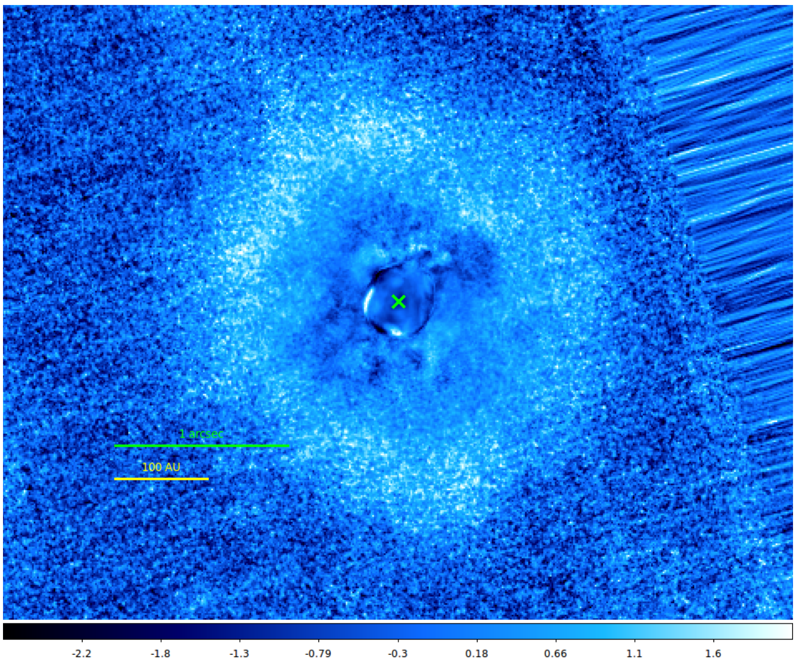

(b) Signal-to-noise

Figure 3.16: Stokes I reduced with the ADI technique and its SNR. The green cross shows the stellar position. The SNR becomes negative due to the negative values in Stokes I from self subtraction.

Chapter 4

Disk Modelling with MCFOST

A good way to learn more about disks is to create a model. This is not an easy task and finding a proper model for a particular disk that reproduces observations is especially challenging. Direct imaging of a disk, like what we have done in Chapter 3, gives us the most direct information about the geometry of a disk at a single wavelength. Limiting spatial resolution together with large inner working angles make it hard to determine the full radial structure of a disk [9]. Therefore, we start from the SED.
Taking the parameters (Table 3.4.1) from our scattered light observations as a starting point, we begin with manually adjusting a model with a single continuous disk so that it fits the SED, varying the dust mass, scale height, inner radius and the exponent of the density distribution. Then we recreate the model Andrews et al. [23] suggested based on their submm visibilities. Both will be described in Section 4.2. Finally, we create simulated H-band polarized intensity images to compare these with our own observations.

4.1 The MCFOST Code

The simulation code we used is called MCFOST. It is a Monte-Carlo three dimensional continuum radiative transfer code (Pinte et al. [37]). For the Monte-Carlo method, individual packages of photons are allowed to propagate through the disk. Their path is governed by the interactions they have with the environment. The photons can undergo scattering, absorption and re-emission events and their occurence depends on the properties of the disk like the opacity.
There are two main sources of radiation in MCFOST, either thermal emission from dust in the disk, or photospheric emission from the star.
The thermal emission is assumed to be isotropic and depends on the temperature, density and opacity of the material. The stellar emission is governed by the stellar spectrum. Photon packages that manage to escape the computation grid are used to determine the SED and create simulated images. The code goes through two stages for the full calculation of the SED. First it determines the temperature distribution in the disk by letting photon packages from the photosphere, each with the same amount of energy, interact with the disk. Because these are random processes, a sufficient number of photon packages needs to be used to converge the temperature estimation. Figure 4.1 shows the effect of this. If only a hundred photon packages are used (right), the temperature profile shows individual tracks of the photons, giving a noisy result. The number of required photons depends on the model itself. Optically thick disks require more photon packages to penetrate the optically thick regions and still provide sufficient statistics to calculate the dust temperature.

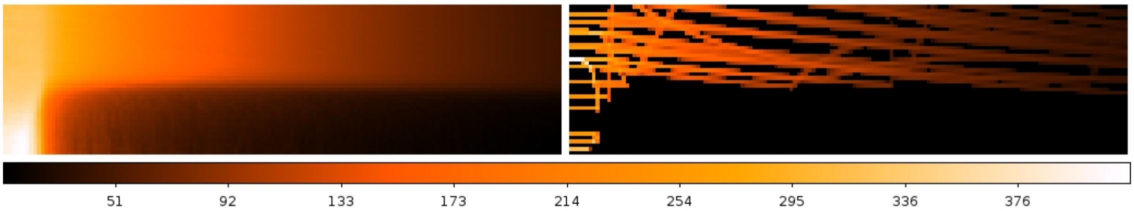

Figure 4.1: Temperature profile for an MCFOST model using 10^6 photon packages (left) and 100 photon packages (right). The latter clearly shows the tracks of individual photon packages. The colorscale gives the temperature, the vertical axis denotes the height within the disk and the horizontal axis the radius.

The temperature profile can then be used for calculating the SED. In this step the number of photon packages that are emitted at each wavelength is kept constant. This makes the energy of a photon package dependant on the wavelength at which it is emitted, ensuring the noise level at each wavelength is comparable and increasing the efficiency of the SED calculation. Rather than being able to be absorbed, scattered or re-emitted, the photon packages are now only allowed to scatter. The code then compensates for the amount of energy that would otherwise have been removed by absorption by weighting the energy of the photon packages with the probability of scattering. For imaging MCFOST, follows a similar strategy, calculating the images at one specific wavelength and keeping track of the Stokes parameters as well. This makes it possible for us to create simulated polarized intensity images for our models.

4.2 Two Models

The SED of RXJ1615 can be constructed by using photometric data spanning from the optical to the millimeter regime from the literature. We give these fluxes in Table 4.1 with their errors and the corresponding references. Most of the fluxes in the optical and near-IR are given in the magnitude system. These need to be converted to regular flux units with the zero-magnitude (see Equation 3.13). In some cases, two references were available with slightly different flux levels at the same wavelengths. Wahhaj et al. [38] reduced the same Spitzer mid- and far-IR data as Padgett et al. [39], but Wahhaj et al. [38] used a new, standardized pipeline to do the data reduction. For completeness, we list both those values in Table 4.1. Furthermore, reddening due to interstellar dust also affects the flux levels, mostly in the optical. We de-reddened the data using the Cardelli, Clayton, and Mathis [40] reddening law (CCM) with an extinction $A_V = 0.4$ and R_V=5 taken from Andrews et al. [23].

Wavelength (μm)	Flux (mJy)	1-σ Error (mJy)	Reference	Zero-magnitude Flux (Jy)
0.36 (U-band)	5.1	0.2	[20]	1810 [41]
0.44 (B-band)	22.0	0.4	*	4260 [41]
0.55 (V-band)	57.7	0.5	*	3640 [41]
0.64 (R_c-band)	101.1	0.9	*	3080 [41]
0.79 (I_c-band)	160.9	1.5	*	2550 [41]
0.55	55.6	1.5	[39]	
0.64	94.7	2.6	*	
0.79	155.1	4.3	*	
1.235 (J-band)	268.2	5.9	[20]	1594 [42]
1.662 (H-band)	315.9	6.7	*	1024 [42]
2.159 (K_s-band)	251.6	4.4	*	666.7 [42]
3.6	98.0	4.9	[38]	
4.5	85.0	4.3	*	
5.8	65.0	3.3	*	
8.0	73.0	3.7	*	
24.0	322.0	32.2	*	
70.0	1049.0	167.0	*	
3.6	114.0	17.1	[39]	
4.5	85.0	12.8	*	
5.8	61.0	9.2	*	
8.0	66.0	9.9	*	
24.0	271.0	40.7	*	
70.0	727.0	145.4	*	
880	430.0	2.8	[23]	
1300	132.0	3.9	[43]	
3200	6.7	0.6	*	

Table 4.1: Photometric data from the literature with applied zero-points. These fluxes have not yet been corrected for reddening. A '*' means that the reference is the same as the line above it.

We also looked into including a couple of data points from the Spitzer Infrared Spectrograph (IRS) around the 10 μm silicate feature. This is a small emission band in the SED at $\sim$10 μm coming from small dust grains in the surface layer of the disk [44]. Different types of silicates produce different shapes of the feature [44], making its occurence very sensitive to the adopted grain composition and size in the model. For this reason it is challenging to get a good fit of the silicate feature without having a detailed look at the dust composition in the disk, sometimes requiring a specific mix of different species to get the right shape of the silicate feature [45]. Therefore, we do not consider the silicate feature when trying to fit our models, but rather include it in the plot for completeness. The fluxes were taken from Evans et al. [46] through the Spitzer IRS online database. The values are given in Table 4.2.

Wavelength (μm)	Flux (mJy)	1-σ Error (mJy)
9.51	132.9	2.3
10.06	157.0	2.0
10.54	166.1	2.1
11.02	171.2	2.7
11.51	148.2	2.6

Table 4.2: Spitzer IRS spectrum fluxes [46] around the $\sim$10 μm silicate feature, and their respective error. The values are directly taken from the spectrum at these specific wavelengths without binning.

Before we move into the specific models, we need to introduce some of their general properties.

- Both models are axisymmetric and defined on a cyllindrical grid
- The density structure follows a Gaussian profile with scale height H:

$$\rho(r,z) = \rho_0(r)e^{-\frac{z^2}{2H(r)^2}} \tag{4.1}$$

- The scale height is allowed to "flare up", so that more surface area is exposed to the stellar light than for a flat disk. This is characterized by the flaring exponent β

$$H(r) = H_0\left(\frac{r}{r_0}\right)^{\beta} \tag{4.2}$$

  where r_0 is a reference radius which can be chosen arbitrarily together with the scale height at that point H_0.

- The surface density is either set to a power law-distribution, or a tapered edge one, where the power-law is cut off by an exponential. The latter follows from work done on viscous accretion disk models [3]. Both are characterized by the surface density exponent ϵ:

  - Power-law:

$$\Sigma(r) = \Sigma_0\left(\frac{r}{r_0}\right)^{\epsilon} \tag{4.3}$$

    Here Σ_0 denotes the surface density at the reference radius r_0
  - Tapered edge:

$$\Sigma(r) = \Sigma_c\left(\frac{r}{R_c}\right)^{\epsilon} e^{-\left(\frac{r}{R_c}\right)^{2-\epsilon}} \tag{4.4}$$

    With R_c the characteristic radius from which the exponential in the distribution becomes important and Σ_c the surface density at that point.

- The dust grain population follows a power-law distribution of the grain size s, ranging from the smallest size s_{min} to the largest s_{max} grains:

$$n(s) \propto s^{-3.5} \tag{4.5}$$

4.2.1 Stellar parameters

For both of the models we used the same stellar spectrum. Most of the parameters were available from Andrews et al. [23], but because MCFOST uses a standard set of input spectrum files, we needed to slightly alter some of the values. For example, the temperature of the star was decreased from 4350 K to 4200 K because that was the best fitting spectrum available in the database of MCFOST. This required a slight increase in the stellar radius to keep the same stellar luminosity of 1.3 $L_{\odot}$. The adapted stellar parameters are listed in Table 4.3.

Parameter	Value
Spectral type	K5
T_{eff}	4200 K
$R_{\star}$	$2.16 R_{\odot}$
$M_{\star}$	$1.10 M_{\odot}$
distance	185 pc

Table 4.3: Stellar parameters adapted from Andrews et al. [23] to be used in MCFOST.

4.2.2 Single-zone Disk Model

The first disk model we attempted to fit to the SED consists of a simple single-zone, continuous disk that is truncated at a radius R_{in} close to the star. The surface density is given by a power-law (Equation 4.3) and we fixed the inclination angle i and the outer radius R_{out} at the values found from our scattered light images (see Section 3.4). We then manually tried to adjust the other parameters (dust mass, scale height, inner radius, etc.) until we got a satisfactory result. The resulting SED is given in Figure 4.2 and its parameters are summarized in Table 4.4.

Parameter	Value
Surface density distribution type	Power-law
M_{dust}	$7{\cdot}10^{-4}\ M_{\odot}$
H(100 AU)	3.5 AU
R_{in}	2.7 AU
R_{out}	92 AU
β	1.3
ϵ	1.5
s_{min}	0.005 μm
s_{max}	1 mm
i	31.8°

Table 4.4: Model parameters for the simple single-zone disk model.

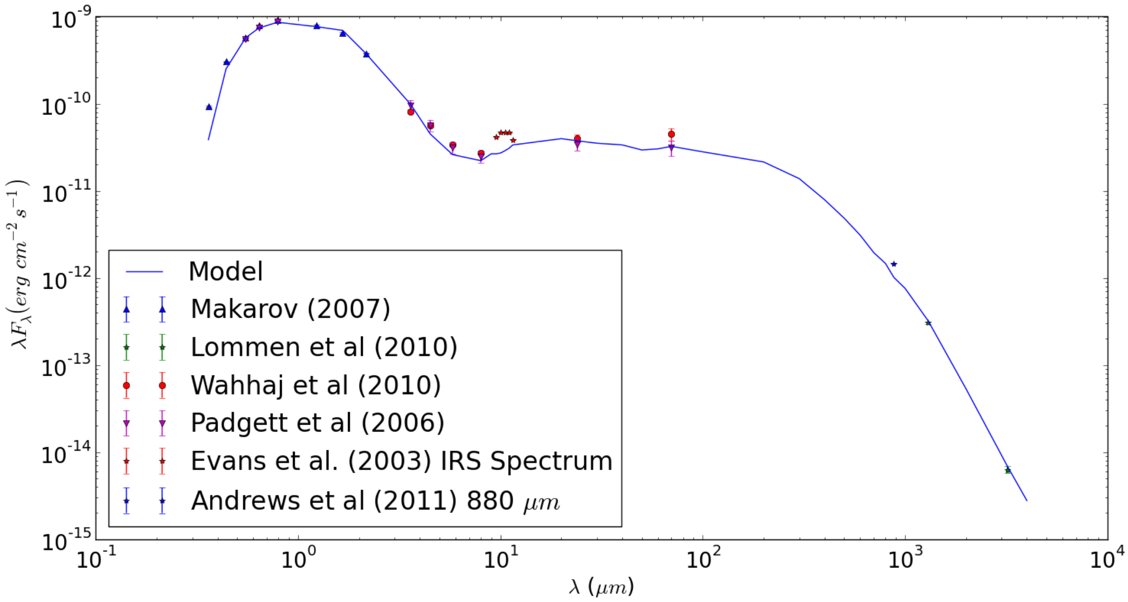

Figure 4.2: SED for the single-zone disk model. The parameters are given in Table 4.4. The different markers denote the photometric points from different references. The fluxes from Table 4.1 have been de-reddened in this plot. The large difference in the two data points at 70 μm comes from the different data reduction pipelines used by Padgett et al. [39] and Wahhaj et al. [38].

4.2.3 More Zones, More Parameters

Andrews et al. [23] suggested a more complicated model. This consists of an inner disk, an outer disk and a gap in between the two. Their surface density follows the tapered edge profile (Equation 4.4), but in the inner regions they supress the surface density to allow for a low density cavity that represents the dip in intensity in their submm data (see Figure 2.1). So within the cavity $\Sigma(\mathrm{R} \leq R_{cav}) = \delta_{cav}\Sigma(R)$ with $\log \delta_{cav} = -5.8$.
Then they introduce a "wall" on the inside of the outer disk. This is a narrow ($\Delta R = 0.1$ AU) region where they locally increased the scale height. Because at the edge of the disk, a lot of material is directly exposed the stellar radiation field, heating up that region and causing it to be puffed up [47].
Furthermore, they allow for dust settling [48], where the larger dust grains "sink" down towards the midplane. They mimick this effect by creating two separate density distributions for the outer disk, one for small grains and one with a decreased scale height for larger grains (see Table 4.5). Then they put 85% of the mass in the large grains and the remaining 15% into the small ones. To clarify the structure of this model, we show a sketch of it in Figure 4.3.

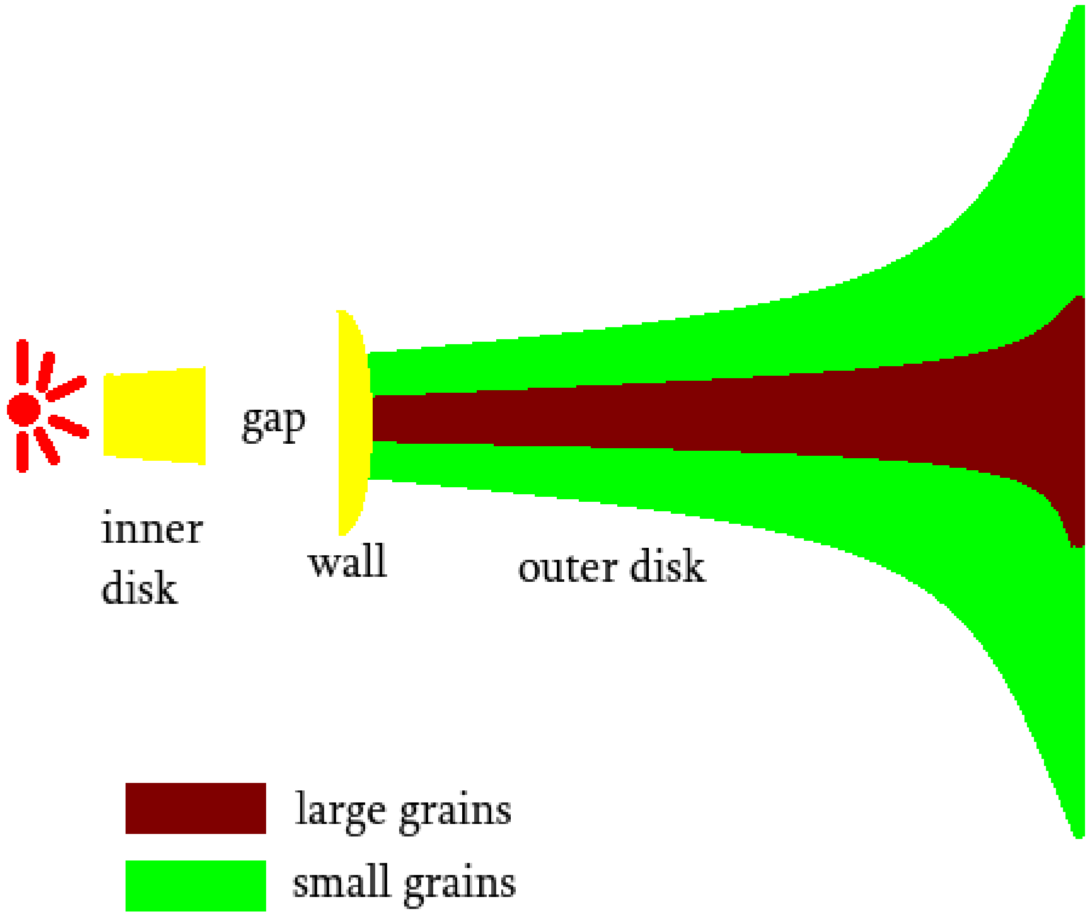

Figure 4.3: A sketch of the Andrews et al. [23] model.

Converting all their parameters into MCFOST proved to be complicated. Because the effect of the inclination angle on the SED is small, except for edge-on disks, and because this proved to be more convenient in MCFOST, we adopt the same angle as for the single-zone model (31.8°). To allow for the different dust distributions and both the inner disk and the wall, it is necessary to introduce four zones. Each zone represents a different component and has its own density structure and dust grain distribution. MCFOST also requires setting the dust mass for each of them. However, Andrews et al. [23] only specify the total mass of the disk ($M_{disk} = 0.128\ M_{\odot}$). To convert this to a dust mass, we assume an interstellar gas-to-dust ratio of 100. This gives us a total dust mass of $M_{dust} = \frac{M_{disk}}{101}$, which should be equal to the integral over the surface density in Equation 4.4.

Using the assumption Andrews et al. [23] make, of a surface density exponent $\epsilon = 1$, this gives:

$$\begin{aligned} M_{dust} &= \int\limits_{R_1}^{R_2} \Sigma(r) \cdot 2\pi r dr \\ &= 2\pi\Sigma_c \int\limits_{R_1}^{R_2} \left(\frac{r}{R_c}\right)^{\epsilon} r e^{-\left(\frac{r}{R_c}\right)^{2-\epsilon}} dr \\ &= -2\pi\Sigma_c R_c^2 \left[e^{-\frac{r}{R_c}}\right]_{R_1}^{R_2} \end{aligned}$$

To include all the different zones, the integral needs to be expanded. If we define

$$Z_i = 2\pi \int\limits_{R_{in}}^{R_{out}} \left(\frac{r}{R_c}\right)^{\epsilon} r e^{-\left(\frac{r}{R_c}\right)^{2-\epsilon}} dr \tag{4.6}$$

as the integral over the surface density profile for an individual zone from its inner radius R_{in} to the outer radius of the zone R_{out} (note that the inner disk would still require a multiplication with δ_{cav}), then we can solve for Σ_c:

$$\begin{aligned} \Sigma_c &= \frac{M_{dust}}{\sum\limits_i Z_i} \\ &= \frac{M_{dust}}{\delta_{cav} \cdot Z_{inner\,disk} + Z_{wall} + 0.85 \cdot Z_{outer\,disk} + 0.15 \cdot Z_{outer\,disk}} \end{aligned}$$

The mass of each zone m_i can then be calculated accordingly, where for the outer radius of the outer disk we took 920 AU, which is the radius MCFOST takes when choosing this tapered edge model.

$$m_i = \alpha_i \Sigma_c Z_i \tag{4.7}$$

Here α_i equals 0.85 for the large grains in the outer disk, 0.15 for the small grains in the outer disk, unity for the wall and δ_{cav} for the inner disk. Applying these equations did not seem to completely reproduce the SED however and we needed to increase the mass of the inner disk by a factor of 10 and decrease the mass of the wall by a factor of 100. We list the full set of parameters for each section separately in Table 4.5 and the SED model in Figure 4.4. The MCFOST parameter files for both models can be found in Appendix B.

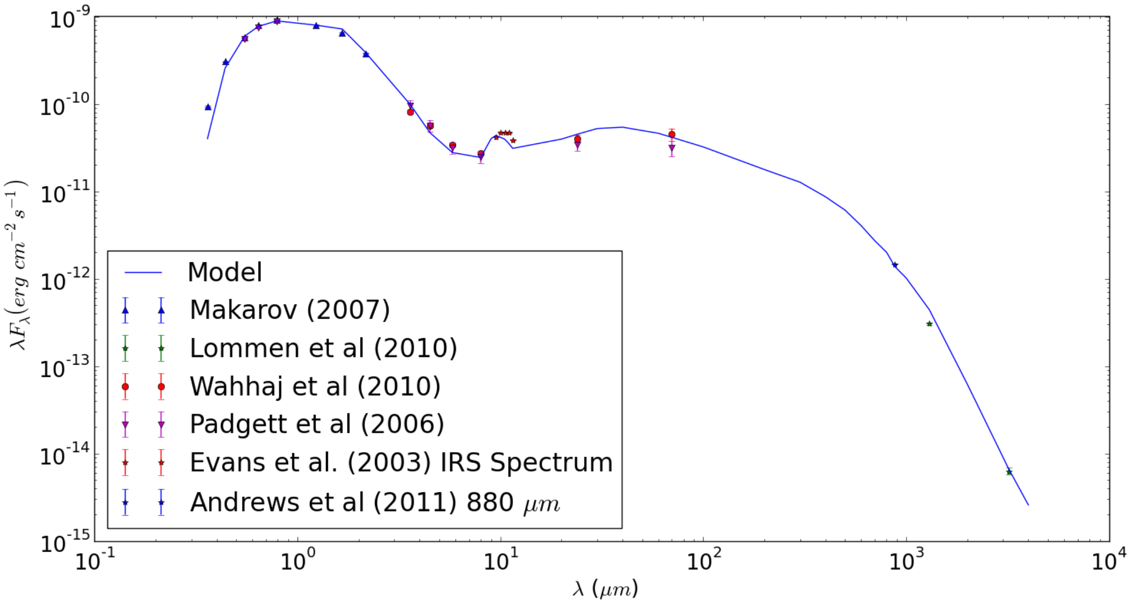

Figure 4.4: SED for the multi-zone disk model. The parameters are given in Table 4.5. The different markers denote the photometric points from different references. The fluxes from Table 4.1 have been de-reddened in this plot.

(a) Inner disk, only small grains

Parameter	Value
$\Sigma(r)$ distribution type	Power-law
M_{dust}	$2.06 \cdot 10^{-9} M_\odot$
H(100 AU)	3.4 AU
R_{in}	0.5 AU
R_{out}	10.0 AU
β	1.25
ϵ	1
s_{min}	0.005 μm
s_{max}	0.25 μm

(b) Wall, only small grains

Parameter	Value
$\Sigma(r)$ distribution type	Power-law
M_{dust}	$1.10 \cdot 10^{-8} M_\odot$
H(30 AU)	2.0 AU
R_{in}	30.0 AU
R_{out}	30.1 AU
β	1.25
ϵ	1
s_{min}	0.005 μm
s_{max}	0.25 μm

(c) Outer disk, small grains

Parameter	Value
$\Sigma(r)$ distribution type	Tapered edge
M_{dust}	$1.90 \cdot 10^{-4} M_\odot$
H(100 AU)	3.4 AU
R_{in}	30.1 AU
R_c	115 AU
β	1.25
ϵ	1
s_{min}	0.005 μm
s_{max}	1 μm

(d) Outer disk, large grains

Parameter	Value
$\Sigma(r)$ distribution type	Tapered edge
M_{dust}	$1.08 \cdot 10^{-3} M_\odot$
H(100 AU)	0.68 AU
R_{in}	30.1 AU
R_c	115 AU
β	1.25
ϵ	1
s_{min}	0.005 μm
s_{max}	1 mm

Table 4.5: Model parameters for Andrews et al. [23] model. Each disk section is shown separately.

4.3 Results from Simulated Images with MCFOST

As was mentioned in Section 4.1, MCFOST also has the capability to simulate images of the disk models. It puts the disk model at the desired distance (185 pc) and then determines the resulting image for a single wavelength. We use this to produce an 880 μm continuum image for both of the models. Because MCFOST also keeps track of the Stokes parameters, it is also possible to create H-band polarized intensity images. However, the images the code produces do not take the effects from observing with a telescope into account. Determining this point spread function (PSF) accurately requires knowledge of all the telescope optics, other instrumental effects and the seeing. The final observational result is given by a convolution of the image with the PSF, causing the image to be smeared out.

4.3.1 H-band

Because we do not have a specific PSF for H-band observations with the Subaru telescope, we estimate the PSF by a two-dimensional Gaussian profile:

$$PSF(r) = \frac{1}{2\pi\sigma^2} e^{-\left(\frac{r^2}{2\sigma^2}\right)} \tag{4.8}$$

Here $r = \sqrt{x^2 + y^2}$ denotes the radius in the image in pixels measured from the central pixel and σ gives the width of the profile. The latter is determined from the FWHM, which is given by:

$$FWHM = 2\sqrt{2\ln 2}\sigma \tag{4.9}$$

For our data set, we removed all images where the FWHM of the stellar PSF became larger than 16 pixels, or 0.152 arcsec (see Section 3.2.8). Therefore, we choose this as the FWHM for the PSF with which to convolve the images in the H-band. For the position angle of the disk, we adopt the value from our H-band observations for the single zone model (33.9°) and the value of Andrews et al. [23] (37°) for the multi-zone model. Calculating PI from the simulated Stokes Q and U parameters (Equation 1.8) and convolving it with the PSF gives the images in Figure 4.5.

4.3.2 880 micron

For the submm images we apply the same strategy as for the H-band, but now taking the total intensity images instead of polarized intensity. For the FWHM of the PSF we adopt the average size of the dimensions of the elliptical telescope beam from Andrews et al. [23] (0.52 arcsec by 0.26 arcsec), giving an FWHM of 0.195 arcec. The results can be found in Figure 4.6.

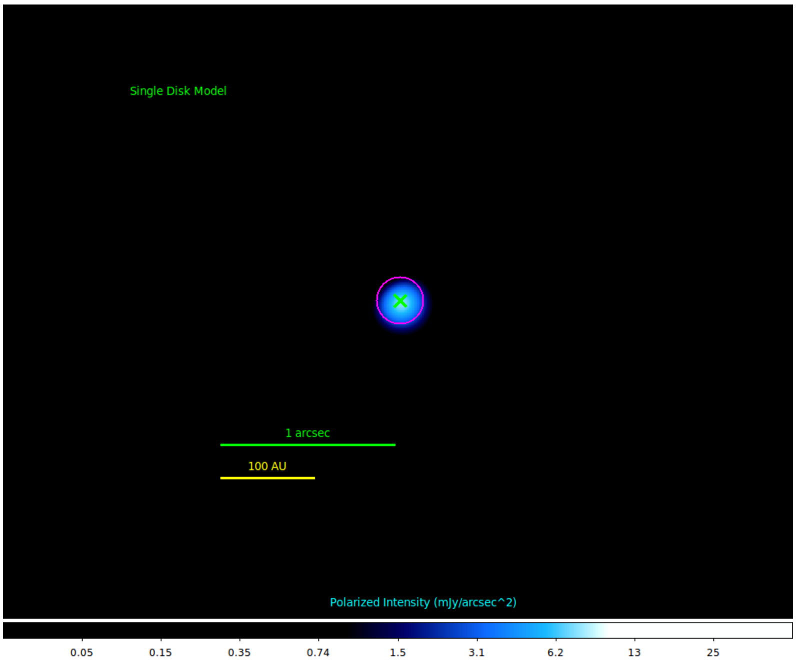

(a) Single-zone disk model

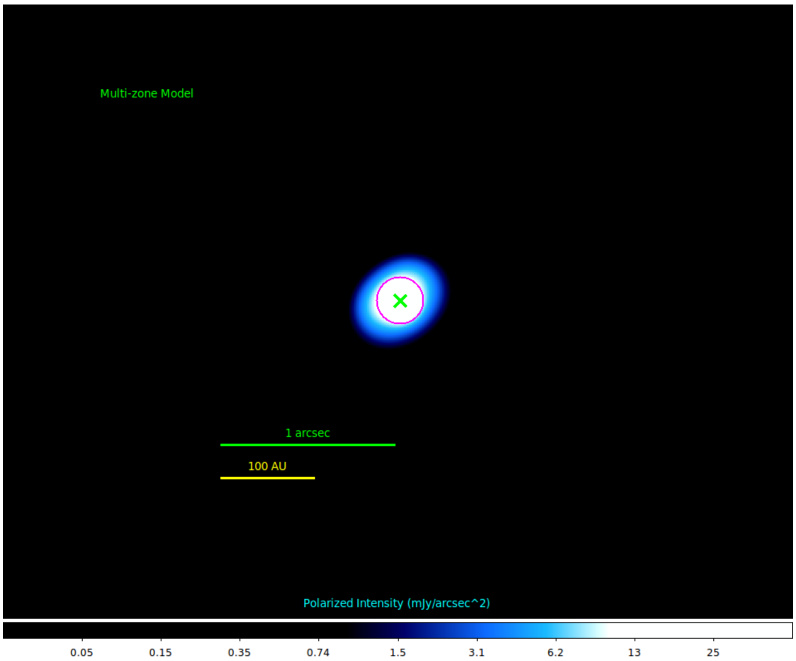

(b) Multi-zone disk model

Figure 4.5: Simulated H-band Polarized Intensity images for both models, convolved with a Gaussian PSF with FWHM = 0.152 arcec. The scales are identical to Figure 3.14. The green cross gives the stellar position and the magenta circle denotes the inner working angle from our H-band observations.

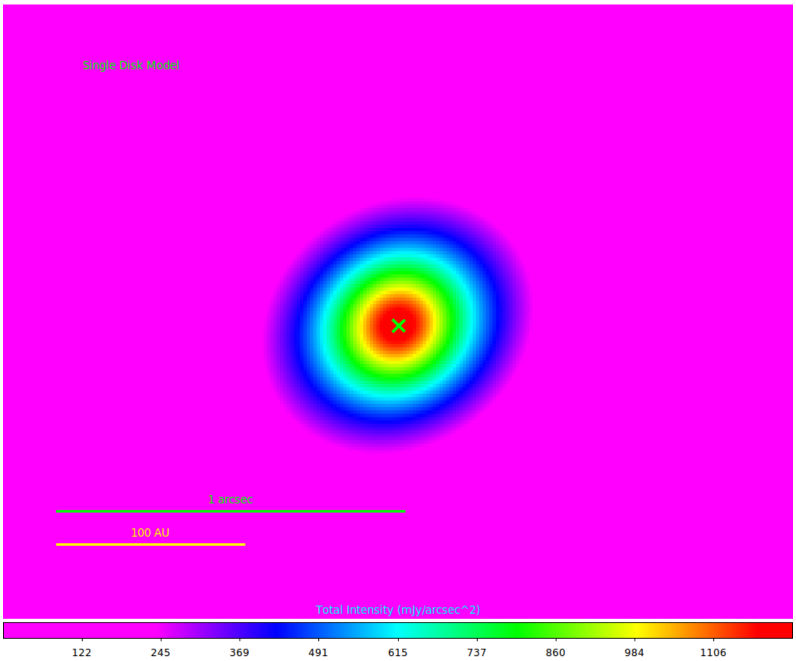

(a) Single-zone disk model

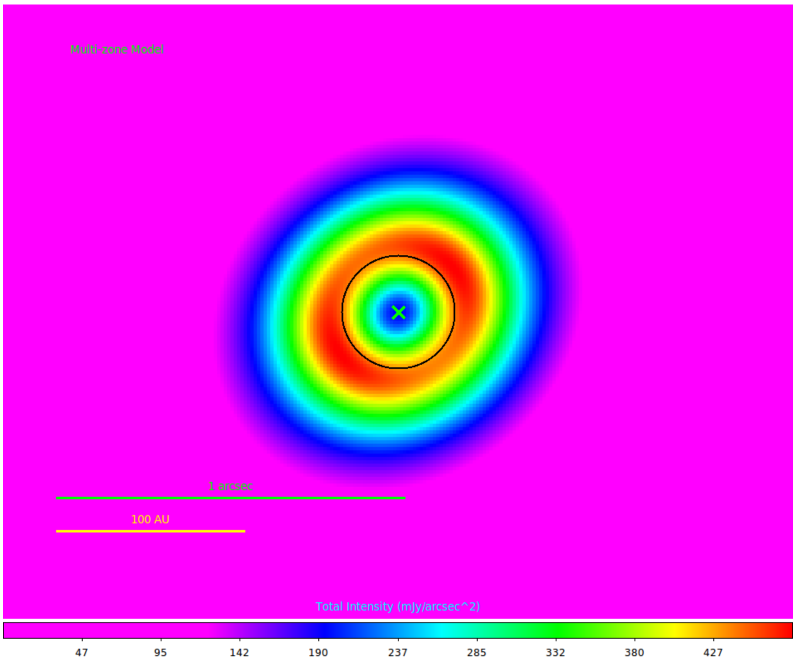

(b) Multi-zone disk model

Figure 4.6: Simulated 880μm images for both models, convolved with a Gaussian PSF with FWHM = 0.195 arcsec. The stellar position is at the point of the green cross and the black circle gives the cavity radius of 30 AU.

4.4 Discussion

Both of our models are based on the SED and although they both fit the SED, the obvious difference is the lack of a silicate feature in the single-zone disk model. We already mentioned not having taken the data points from the Spitzer IRS spectrum into account in Section 4.2. Due to the dependence of the feature on the dust grain composition and size, there are many ways to produce a silicate feature in the SED by adding small grains of mixed types to the optically thin top layers of the disk [45]. This also brings up a general problem with fitting the SED through disk models.

The model parameters suffer from multiple degeneracies. As evidenced by our model SEDs, two different model structures with different parameters can produce a fit of the SED. The different components of a multi-zone disk model all affect the SED in a different way, but together they can produce a substantial amount of possible models [23]. Many degeneracies also exist in the structure parameters themselves. For example, both the disk mass and the scale height affect the (sub)mm part of the SED in the same way [49]. Although performing a grid around the parameters can be used to statistically find a best fit, the shear amount of parameters will require fixing some of them. Therefore, combining the SED with multiple other observables like the submm visibilities from Andrews et al. [23] and our scattered light observations is essential for getting constraints on the models.

4.4.1 Simulated Images

Looking at the simulated H-band images for both our models, we see significantly less emission from the single-zone disk model compared to the multi-zone model. Most of the scattered light from the single-zone model comes from the region close to the star and within the inner working angle of our observations (see Figure 4.5a). Due to the flatness of the disk, the surface area from which the light can be scattered is small. Furthermore, because the single-zone disk extends to an inner radius much closer to the star. Therefore, the amount of area that can scatter photons at the inner rim of the disk is smaller than in the multi-zone model. The multi-zone model however, does produce more extended emission in the H-band (Figure 4.5b). Although the emission does not extend as far as is visible in our observations, the brightness outside the inner working angle is comparable. Measured on the major axis, at a radius of ~ 35 AU (taking the mean of both sides), the polarized intensity for the multi-zone model is ~ 5.6 mJy/$arcsec^2$ versus a value of ~ 5.7 mJy/$arcsec^2$ we find for our observations. Another notable feature is that the cavity in the multi-zone disk model is not resolved in the simulated H-band images. Therefore, more work is required to decrease the inner working angle of the scattered light observations to be able to confirm if there is also a cavity present for the small dust grains.

The multi-zone disk model is also able to reproduce the decrease in intensity close to the center seen in the submm visibilities (Figure 4.6a). The shape of the peaks of the cavity wall seems to be more elongated in the simulated images, but because we used a circular PSF to convolve the images with, a direct comparison is limited. Due to the small inner radius of the single-zone disk model, no central decrease in intensity, as in Figure 2.1, shows up in the simulated 880 μm image. This confirms the need for more than just the SED as the basis of a disk model.

4.4.2 Disk Stability

Because both disk models have a high mass and a low scale height, the disk can be expected to become susceptible to gravitational instabilities. To investigate this possibility, we use the Toomre Q parameter [2] given by

$$Q = \frac{c_s \Omega}{\pi G \Sigma} \tag{4.10}$$

G is the gravitational constant, c_s the local sound speed, Σ the surface density and Ω the orbital frequency. If Q $\leq$ 1, self-gravity in the disk is important and the disk possibly fragment and form planetesimals [2]. For the calculation, we assume Keplerian rotation, given by

$$\Omega_k = \sqrt{\frac{GM_\star}{r^3}} \tag{4.11}$$

with $M_\star$ the stellar mass and r the radius. The local sound speed is determined from the disk temperature at the midplane through

$$c_s = \sqrt{\frac{k_B T_{midplane}}{\mu m_H}} \tag{4.12}$$

where m_H is the hydrogen mass, k_B is the Boltzmann constant and μ is the mean molecular weight. For μ, we assume a value of 2.4, which is valid for molecular gas of solar composition [50]. We take the midplane temperature from the temperature profile of our models and also directly use the gas surface density from the MCFOST output, assuming a gas-to-dust ratio of 100. Plots of the gas surface density profiles for the single-zone model and the multi-zone model are given in Figures 4.7a and 4.8a, respectively. The midplane temperature is shown in Figures 4.7b and 4.8b. The single-zone disk model has a sharp decrease in the temperature at $\sim$ 5 AU due to the presence of a very optically thick region. The puffed up wall in the multi-zone model also has a high temperature due to the large surface area directly illuminated by the star. Following from Equation 4.10, the Toomre Q parameter is shown in Figures 4.7c and 4.8c.

In both models the Toomre Q parameter stays well above unity throughout the disk. In the highly optically thick region of the single-zone disk model, the Q parameter does drop rapidly, but it stays above unity. The temperature increases sharply in the regions close to the star, becoming too hot for self-gravity to get a hold and driving the Q parameter up to very high values. This means that the entire disk is stable against self-gravity and the formation of planetesimals through a gravitational instability seems unlikely for these two disks models.

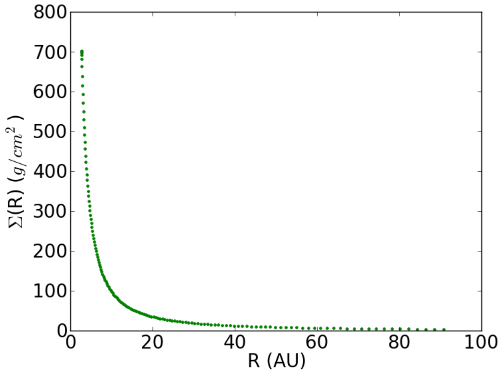

(a) Gas Surface Density

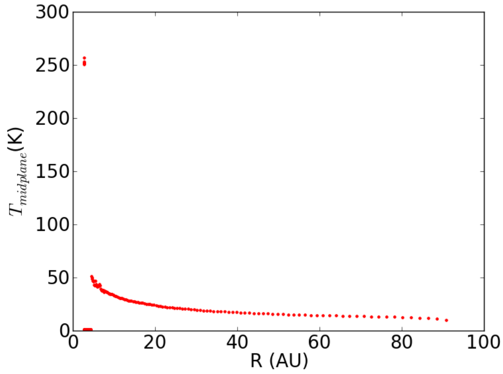

(b) Midplane Temperature

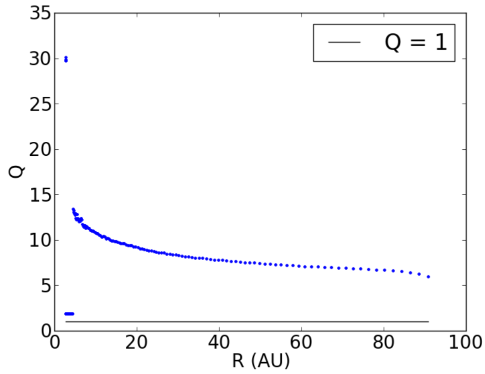

(c) Toomre Q

Figure 4.7: Radial plots of the disk midplane temperature, gas surface density and Toomre Q parameter for the single-zone disk model. The midplane temperature at the inner radius extends out to ~550 K and the dip in the temperature profile is due to a very optically thick region present there in the disk. The temperature profile could therefore not converge in that region without more photon packages.

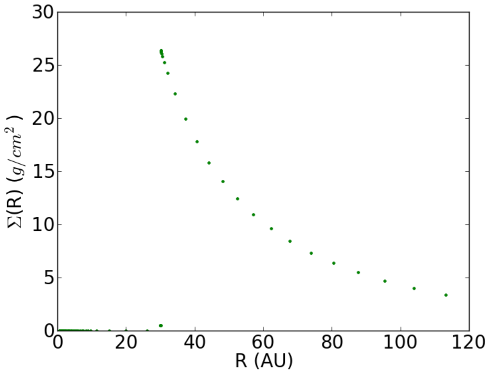

(a) Gas Surface Density

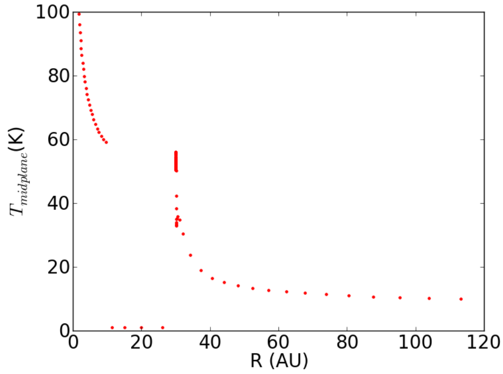

(b) Midplane Temperature

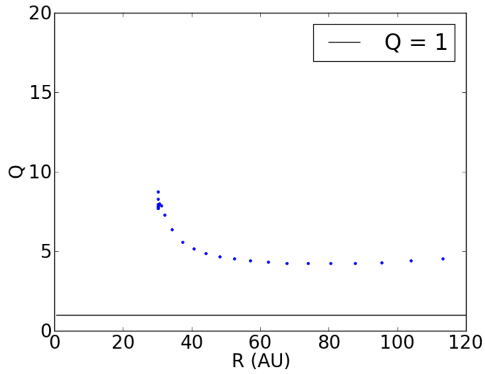

(c) Toomre Q

Figure 4.8: Radial plots of the disk midplane temperature, gas surface density and Toomre Q parameter for the multi-zone disk model. The Toomre Q parameter reaches extremely large values of $\sim 10^6 - 10^7$ for the inner disk, falling of the scale in that plot.

Chapter 5

Conclusion

In this thesis we studied the transitional disk RX J1615.3-3255 with the goal of charactarizing the disk structure from the dust emission. We performed a two stage analysis, starting with H-band scattered light observations . Then we created two disk models, a single-zone, continuous disk and a multi-zone model with a cavity and puffed up cavity wall based on the model from Andrews et al. [23]. From these models, we produced simulated images to compare with our observations and submm images from the literature. The important conclusions are summarized below:

- We have detected the polarized extended disk emission in the H-band scattered light observations with an outer radius of 92 $\pm$ 12 AU. Our observations do not show signs of dust depletion in the inner regions of the disk, possibly pointing to smaller dust grains extending to distances closer to the star than the large grains. We also do not see any structure in the emission, such as clumps or spiral arms.

- Although both models fit the SED, the multi-zone model seems to be the most realistic, being able to reproduce both the central decrease in intensity observed at 880 μm and the polarized intensity in the H-band scattered light.

- Both models show stability against self-gravitation throughout the entire disk, assuming a gas-to-dust ratio of 100. If the cavity observed in the submm is the effect of a planet orbiting close to the star, it is unlikely that this was formed through the gravitational instability.

5.1 Future Work

There are several things that can still be done to improve or expand on the work presented in this thesis. To allow for a more accurate comparison of the scattered light in the observations with that in the simulated H-band images, we would need to simulate all the effects of observing with Subaru and HiCIAO. This needs to be done because the telescope PSF is not necessarily circular. Another effect is that of instrumental polarization on the simulated observations. Although we did correct for this in our observations, the method is not infallible and some small amounts of artificial polarization could still be present in the data [13]. Furthermore, the current analysis relies on inferring observational effects, such as the PSF, from the observed image. Performing our analysis of the disk models with detailed Subaru telescope simulations allows us to trace the effect of each telescope component separately and could improve the accuracy of our results.

So far, everything we have discussed in this thesis, except for the Toomre Q parameter, concerned the dust in the disk without touching upon the gas. For Q we have assumed a gas-to-dust ratio of 100 to estimate the gas content. However, this assumption does not necessarily have to hold and the gas could display different behavior [51]. It would be meaningful to see if the gas is also cleared in the cavity and if its distribution traces the small or large dust grains. Moreover, a measurement of the gas density distribution would allow us to determine if the disk is able to form planets through gravitationally instability or not. Therefore, molecular line observations (The CO J=3-2 line for example) with the Atacama Large Millimeter Array (ALMA) could help give better constraints on the planet formation capabilities of RX J1615.3-3255.

5.2 Acknowledgements

The work presented in this thesis would not have been possible without the continued support of a number of people. First and foremost, I would like to extend my sincerest gratitude to both my supervisors, Inga Kamp and Misato Fukagawa. They have truly been inspirational to work with, always showing enthousiasm and always willing to take the time to explain all the necessary concepts in detail. Over the course of two years I feel that I have learned a lot from working with both of them. Much gratitude also goes out to Hiroshi Shibai, who allowed me to work in the IRAL lab and go through this incredible experience. Special thanks go to Matthias Samland and Balaji Muthusubramanian. Their friendship has been exceptional and the useful discussions we had were a key factor in working through multiple stages of this research project. I would also like to thank Yayoi Maruta and the other members of the IRAL lab for their kindness and amazing hospitality. Finally, I would like to extend gratitude to the following people for all the support they have given: Pablo Riviere, Stefano Antonellini, Francois Menard, Christophe Pinte, Sander Bus, Wing-Fai Thi, Peter Woitke, Andrés Carmona Gonzales, Leonie van Helvert and Mark Erends.

Bibliography

[1] S. Udry and N. C. Santos. Statistical Properties of Exoplanets. ARA&A, 45:397–439, September 2007. doi: 10.1146/annurev.astro.45.051806.110529.

[2] Philip J. Armitage. *Astrophysics of Planet Formation*. Cambridge University Press, 2010.

[3] J. P. Williams and L. A. Cieza. Protoplanetary Disks and Their Evolution. ARA&A, 49: 67–117, September 2011. doi: 10.1146/annurev-astro-081710-102548.

[4] S. M. Vicente and J. Alves. Size distribution of circumstellar disks in the Trapezium cluster. A&A, 441:195–205, October 2005. doi: 10.1051/0004-6361:20053540.

[5] N. Grosso, J. Alves, K. Wood, R. Neuhäuser, T. Montmerle, and J. E. Bjorkman. Spatial Study with the Very Large Telescope of a New Resolved Edge-on Circumstellar Dust Disk Discovered at the Periphery of the ρ Ophiuchi Dark Cloud. ApJ, 586:296–305, March 2003. doi: 10.1086/367557.

[6] Floris van der Tak. Star and Planet Formation, Slides of Lecture 8, 2014.

[7] C. J. Lada. Star formation - From OB associations to protostars. In M. Peimbert and J. Jugaku, editors, *Star Forming Regions*, volume 115 of *IAU Symposium*, pages 1–17, 1987.

[8] P. Andre, D. Ward-Thompson, and M. Barsony. Submillimeter continuum observations of Rho Ophiuchi A - The candidate protostar VLA 1623 and prestellar clumps. ApJ, 406: 122–141, March 1993. doi: 10.1086/172425.

[9] C. Espaillat, J. Muzerolle, J. Najita, S. Andrews, Z. Zhu, N. Calvet, S. Kraus, J. Hashimoto, A. Kraus, and P. D'Alessio. An Observational Perspective of Transitional Disks. *ArXiv e-prints*, February 2014.

[10] K. M. Strom, S. E. Strom, S. Edwards, S. Cabrit, and M. F. Skrutskie. Circumstellar material associated with solar-type pre-main-sequence stars - A possible constraint on the timescale for planet building. AJ, 97:1451–1470, May 1989. doi: 10.1086/115085.

[11] C. Espaillat, L. Ingleby, J. Hernández, E. Furlan, P. D'Alessio, N. Calvet, S. Andrews, J. Muzerolle, C. Qi, and D. Wilner. On the Transitional Disk Class: Linking Observations of T Tauri Stars and Physical Disk Models. ApJ, 747:103, March 2012. doi: 10.1088/0004-637X/747/2/103.

[12] J. E. Owen, B. Ercolano, and C. J. Clarke. Protoplanetary disc evolution and dispersal: the implications of X-ray photoevaporation. MNRAS, 412:13–25, March 2011. doi: 10.1111/j.1365-2966.2010.17818.x.

[13] H. Avenhaus, S. P. Quanz, H. M. Schmid, M. R. Meyer, A. Garufi, S. Wolf, and C. Dominik. Structures in the Protoplanetary Disk of HD142527 Seen in Polarized Scattered Light. ApJ, 781:87, February 2014. doi: 10.1088/0004-637X/781/2/87.

[14] Eugene Hecht. *Optics*. Addison Wesley, 4th edition, 2002.

[15] Jaap Tinbergen. *Astronomical polarimetry.* Cambridge University Press, 1st edition, 1996.

[16] Stokes Parameter Image, . URL `http://en.wikipedia.org/wiki/File:StokesParameters.png`.

[17] N. V. Voshchinnikov and E. Krügel. Circumstellar disc of β Pictoris: constraints on grain properties from polarization. A&A, 352:508–516, December 1999.

[18] A. Natta, L. Testi, N. Calvet, T. Henning, R. Waters, and D. Wilner. Dust in Protoplanetary Disks: Properties and Evolution. *Protostars and Planets V*, pages 767–781, 2007.

[19] K. G. Henize. Observations of southern emission-line stars. ApJS, 30:491–550, April 1976. doi: 10.1086/190369.

[20] V. V. Makarov. The Lupus Association of Pre-Main-Sequence Stars: Clues to Star Formation Scattered in Space and Time. ApJ, 658:480–486, March 2007. doi: 10.1086/511261.

[21] J. Krautter, R. Wichmann, J. H. M. M. Schmitt, J. M. Alcala, R. Neuhauser, and L. Terranegra. New "weak-line"–T Tauri stars in Lupus. A&AS, 123:329–352, June 1997. doi: 10.1051/aas:1997163.

[22] B. Merín, J. M. Brown, I. Oliveira, G. J. Herczeg, E. F. van Dishoeck, S. Bottinelli, N. J. Evans, II, L. Cieza, L. Spezzi, J. M. Alcalá, P. M. Harvey, G. A. Blake, A. Bayo, V. G. Geers, F. Lahuis, T. Prusti, J.-C. Augereau, J. Olofsson, F. M. Walter, and K. Chiu. A Spitzer c2d Legacy Survey to Identify and Characterize Disks with Inner Dust Holes. ApJ, 718:1200, August 2010. doi: 10.1088/0004-637X/718/2/1200.

[23] S. M. Andrews, D. J. Wilner, C. Espaillat, A. M. Hughes, C. P. Dullemond, M. K. McClure, C. Qi, and J. M. Brown. Resolved Images of Large Cavities in Protoplanetary Transition Disks. ApJ, 732:42, May 2011. doi: 10.1088/0004-637X/732/1/42.

[24] Physical parameters of Subaru Telescope, . URL `http://www.naoj.org/Observing/Telescope/`.

[25] A Brief History of Subaru, . URL `http://www.naoj.org/NAOJ/history.html`.

[26] Subaru Telescope Instruments, . URL `http://www.naoj.org/Observing/Instruments/`.

[27] HiCIAO Team and SEEDS Team. HiCIAO Performance Report for SEEDS - Final Report -. September 2009.

[28] Y. Hayano, H. Takami, S. Oya, M. Hattori, Y. Saito, M. Watanabe, O. Guyon, Y. Minowa, S. E. Egner, M. Ito, V. Garrel, S. Colley, T. Golota, and M. Iye. Commissioning status of Subaru laser guide star adaptive optics system. In *Society of Photo-Optical Instrumentation Engineers (SPIE) Conference Series*, volume 7736, July 2010. doi: 10.1117/12.857567.

[29] S. Hinkley, B. R. Oppenheimer, R. Soummer, D. Brenner, J. R. Graham, M. D. Perrin, A. Sivaramakrishnan, J. P. Lloyd, L. C. Roberts, Jr., and J. Kuhn. Speckle Suppression Through Dual Imaging Polarimetry, and a Ground-based Image of the HR 4796A Circumstellar Disk. ApJ, 701:804, August 2009. doi: 10.1088/0004-637X/701/1/804.

[30] A short introduction to Angular Differential Imaging, . URL `http://www.mpia.de/homes/thalmann/adi.htm`.

[31] Canada-France-Hawaii Telescope, SkyProbe Archive, . URL `http://www.cfht.hawaii.edu/cgi-bin/elixir/skyprobe.pl?plot&mcal_20120706.png`.

[32] Mauna Kea Weather Center, . URL `http://mkwc.ifa.hawaii.edu/current/seeing/images/20120706.wrf-vs-mkam.timeseries.jpg`.

[33] J. Hashimoto, M. Tamura, H. Suto, T. Kudo, and R. Suzuki. Polarimetric calibration for Nasmyth instrument HiCIAO. 2010.

[34] Photometric standard star reference, . URL `http://www.jach.hawaii.edu/UKIRT/astronomy/calib/phot_cal/ukirt_stds.html`.

[35] A. T. Tokunaga and W. D. Vacca. The Mauna Kea Observatories Near-Infrared Filter Set. III. Isophotal Wavelengths and Absolute Calibration. PASP, 117:1459–1459, December 2005. doi: 10.1086/499029.

[36] A. Garufi, S. P. Quanz, H. Avenhaus, E. Buenzli, C. Dominik, F. Meru, M. R. Meyer, P. Pinilla, H. M. Schmid, and S. Wolf. Small vs. large dust grains in transitional disks: do different cavity sizes indicate a planet?. SAO 206462 (HD 135344B) in polarized light with VLT/NACO. A&A, 560:A105, December 2013. doi: 10.1051/0004-6361/201322429.

[37] C. Pinte, F. Ménard, G. Duchêne, and P. Bastien. Monte Carlo radiative transfer in protoplanetary disks. A&A, 459:797–804, December 2006. doi: 10.1051/0004-6361:20053275.

[38] Z. Wahhaj, L. Cieza, D. W. Koerner, K. R. Stapelfeldt, D. L. Padgett, A. Case, J. R. Keller, B. Merín, N. J. Evans, II, P. Harvey, A. Sargent, E. F. van Dishoeck, L. Allen, G. Blake, T. Brooke, N. Chapman, L. Mundy, and P. C. Myers. The Spitzer c2d Survey of Weak-line T Tauri Stars. III. The Transition from Primordial Disks to Debris Disks. ApJ, 724:835, December 2010. doi: 10.1088/0004-637X/724/2/835.

[39] D. L. Padgett, L. Cieza, K. R. Stapelfeldt, N. J. Evans, II, D. Koerner, A. Sargent, M. Fukagawa, E. F. van Dishoeck, J.-C. Augereau, L. Allen, G. Blake, T. Brooke, N. Chapman, P. Harvey, A. Porras, S.-P. Lai, L. Mundy, P. C. Myers, W. Spiesman, and Z. Wahhaj. The SPITZER c2d Survey of Weak-Line T Tauri Stars. I. Initial Results. ApJ, 645:1283–1296, July 2006. doi: 10.1086/504374.

[40] J. A. Cardelli, G. C. Clayton, and J. S. Mathis. The relationship between infrared, optical, and ultraviolet extinction. ApJ, 345:245–256, October 1989. doi: 10.1086/167900.

[41] M. S. Bessell. UBVRI photometry. II - The Cousins VRI system, its temperature and absolute flux calibration, and relevance for two-dimensional photometry. PASP, 91:589–607, October 1979. doi: 10.1086/130542.

[42] M. Cohen, W. A. Wheaton, and S. T. Megeath. Spectral Irradiance Calibration in the Infrared. XIV. The Absolute Calibration of 2MASS. AJ, 126:1090–1096, August 2003. doi: 10.1086/376474.

[43] D. J. P. Lommen, E. F. van Dishoeck, C. M. Wright, S. T. Maddison, M. Min, D. J. Wilner, D. M. Salter, H. J. van Langevelde, T. L. Bourke, R. F. J. van der Burg, and G. A. Blake. Grain growth across protoplanetary discs: 10 μm silicate feature versus millimetre slope. A&A, 515:A77, June 2010. doi: 10.1051/0004-6361/200913150.

[44] J. Kessler-Silacci, J.-C. Augereau, C. P. Dullemond, V. Geers, F. Lahuis, N. J. Evans, II, E. F. van Dishoeck, G. A. Blake, A. C. A. Boogert, J. Brown, J. K. Jørgensen, C. Knez, and K. M. Pontoppidan. c2d Spitzer IRS Spectra of Disks around T Tauri Stars. I. Silicate Emission and Grain Growth. ApJ, 639:275–291, March 2006. doi: 10.1086/499330.

[45] C. Espaillat, N. Calvet, P. D'Alessio, J. Hernández, C. Qi, L. Hartmann, E. Furlan, and D. M. Watson. On the Diversity of the Taurus Transitional Disks: UX Tauri A and LkCa 15. ApJ, 670:L135–L138, December 2007. doi: 10.1086/524360.

[46] N. J. Evans, II, L. E. Allen, G. A. Blake, A. C. A. Boogert, T. Bourke, P. M. Harvey, J. E. Kessler, D. W. Koerner, C. W. Lee, L. G. Mundy, P. C. Myers, D. L. Padgett, K. Pontoppidan, A. I. Sargent, K. R. Stapelfeldt, E. F. van Dishoeck, C. H. Young, and K. E. Young. From Molecular Cores to Planet-forming Disks: An SIRTF Legacy Program. PASP, 115:965–980, August 2003. doi: 10.1086/376697.

[47] C. P. Dullemond and C. Dominik. Flaring vs. self-shadowed disks: The SEDs of Herbig Ae/Be stars. A&A, 417:159–168, April 2004. doi: 10.1051/0004-6361:20031768.

[48] C. P. Dullemond and C. Dominik. The effect of dust settling on the appearance of protoplanetary disks. A&A, 421:1075–1086, July 2004. doi: 10.1051/0004-6361:20040284.

[49] S. M. Andrews, D. J. Wilner, A. M. Hughes, C. Qi, and C. P. Dullemond. Protoplanetary Disk Structures in Ophiuchus. ApJ, 700:1502–1523, August 2009. doi: 10.1088/0004-637X/700/2/1502.

[50] Steven W. Stahler and Francesco Palla. *The Formation of Stars*. Wiley-VCH, 2004.

[51] T. Birnstiel, C. P. Dullemond, and F. Brauer. Gas- and dust evolution in protoplanetary disks. A&A, 513:A79, April 2010. doi: 10.1051/0004-6361/200913731.

Appendix A

Parameters File Destriping Code

```
// Folders (Directries)
FIDR ../rawdata/            // Folder of Input Raw Data
FCDS CDS/     // Folder for Coarse Destriping
FFDS FDS/     // Folder for Fine Destriping
FCRR CRR/     // Folder for Cosmicray Removal
FDFC DFC/     // Folder for Dark and Flat Correction

// Threshold Values
MAXDL   1000.0    //ADU    // Maximum Dark Level
MINDL   -800.0    //-200.0 //ADU   // Minimum Dark Level
MAXDD    30.0    //100.0    //ADU   // Maximum Standard Deviation of Dark Images
                          //      (30 for COADD=1,  100 for COADD=10)
MINDD       1.0    //ADU    // Minimum Standard Deviation of Dark Images

NRMIM  10000.0    //       // Normalization Value for Flat Images
MAXRS       6.0   //1.4    //NRMIM   // Maximum Relative Sensitivity
MINRS       0.1    //NRMIM // Minimum Relative Sensitivity
MAXDR       10     // Standard Deviation of Relative Sensitivity
MINDR       0.0010   //    // Standard Deviation of Relative Sensitivity

WARMX      50.0    //30.0 //ADU    // Threshold Level of Warm Pixel
THRS1       5.0    //sigma // Threshold Level of Statistical Deviation
THRS2      15.0    //sigma // Threshold Level of Statistical Deviation

TINTC1      0.75   // (30sec/5sec) Correction for Integration Time of Dark
TINTC2      0.17     // Correction for Integration Time of Dark for Photometry

//
//           Mask Definition   //
//
// Halo for Star Images
HALR1   180.0       // Radius of Halo
HALX1   365.6      // Center of Mask
HALY1   1426.3
HALR2   180.0       // Radius of Halo
```

```
HALX2  1001.6     // Center of Mask
HALY2  1433.0
HALR3  180.0      // Radius of Halo
HALX3  1061.7     // Center of Mask
HALY3  741.9
HALR4  180.0     // Radius of Halo
HALX4 1704.4     // Center of Mask
HALY4  743.6

// Halo for Photometry Images
HALR5  0.0     // Radius of Halo
HALX5  485.0     // Center of Mask
HALY5  1470.0
HALR6  0.0     // Radius of Halo
HALX6  1560.0     // Center of Mask
HALY6  1470.0
// Abnormal Spot
HALRS    6.0     // Radius of Spot
HALXS 1068.0     // Center of Mask
HALYS  224.0

// Spider for Star Images
SPDR1  0.0       // Radius of Spider
SPDX1  507.0     // Crossing point 1
SPDY1  1076.0    //
SPDA1   8.83     // Inclination of Spider A1
SPDB1   0.13     // Inclination of Spider B1
SPDW1   0.0      // Width  of Spider

SPDR2  450.0     // Radius of Spider
SPDX2  1574.0    // Crossing point 2
SPDY2  1088.0    //
SPDA2   8.83     // Inclination of Spider A2
SPDB2   0.13     // Inclination of Spider B2
SPDW2   0.0      // Width  of Spider
// Spider for Photometry Images
SPDR3  150.0     // Radius of Spider
SPDX3  437.0     // Crossing point 3
SPDY3  912.0     //
SPDA3    7.5     // Inclination of Spider A3
SPDB3  0.103     // Inclination of Spider B3
SPDW3   0.0      // Width  of Spider

SPDR4  150.0     // Radius of Spider
SPDX4 1500.0     // Crossing point 4
SPDY4  912.0     //
SPDA4    7.5     // Inclination of Spider A4
SPDB4  0.103     // Inclination of Spider B4
SPDW4   0.0      // Width  of Spider

// Frame for Star Images
FRSRR1 1250   // Right  Boundary of Top-Right
FRSRL1 770    // Left   Boundary of Top-Right
FRSRT1 1630   // Top    Boundary of Top-Right
```

```
FRSRB1 1190    // Bottom Boundary of Top-Right

FRSLR1  635    // Right  Boundary of Top-Left
FRSLL1  155    // Left   Boundary of Top-Left
FRSLT1 1630    // Top    Boundary of Top-Left
FRSLB1  1190   // Bottom Boundary of Top-Left

FRSRR2 1950    // Right  Boundary of Bottom-Right
FRSRL2 1460    // Left   Boundary of Bottom-Right
FRSRT2 935    // Top    Boundary of Bottom-Right
FRSRB2  500    // Bottom Boundary of Bottom-Right

FRSLR2  1320   // Right  Boundary of Bottom-Left
FRSLL2  830    // Left   Boundary of Bottom-Left
FRSLT2  935    // Top    Boundary of Bottom-Left
FRSLB2  500    // Bottom Boundary of Bottom-Left

// Frame for dark regions
FRSRR1b 1300    // Right  Boundary of Top-Right
FRSRL1b 730     // Left   Boundary of Top-Right
FRSRT1b 1700    // Top    Boundary of Top-Right
FRSRB1b 1150    // Bottom Boundary of Top-Right

FRSLR1b  650    // Right  Boundary of Top-Left
FRSLL1b  90    // Left   Boundary of Top-Left
FRSLT1b 1700    // Top    Boundary of Top-Left
FRSLB1b  1150   // Bottom Boundary of Top-Left

FRSRR2b 1990    // Right  Boundary of Bottom-Right
FRSRL2b 1430    // Left   Boundary of Bottom-Right
FRSRT2b 1030    // Top    Boundary of Bottom-Right
FRSRB2b  440    // Bottom Boundary of Bottom-Right

FRSLR2b  1350   // Right  Boundary of Bottom-Left
FRSLL2b  750    // Left   Boundary of Bottom-Left
FRSLT2b  1030    // Top    Boundary of Bottom-Left
FRSLB2b  440    // Bottom Boundary of Bottom-Left


// Frame for Photometry
FRPRR1 1200    // Right  Boundary of Top-Right
FRPRL1 817     // Left   Boundary of Top-Right
FRPRT1 1595    // Top    Boundary of Top-Right
FRPRB1 1230    // Bottom Boundary of Top-Right

FRPLR1  580    // Right  Boundary of Top-Left
FRPLL1  180    // Left   Boundary of Top-Left
FRPLT1 1625    // Top    Boundary of Top-Left
FRPLB1  1200   // Bottom Boundary of Top-Left

FRPRR2 1930    // Right  Boundary of Bottom-Right
FRPRL2 1500    // Left   Boundary of Bottom-Right
FRPRT2 930    // Top    Boundary of Bottom-Right
FRPRB2  500    // Bottom Boundary of Bottom-Right
```

```

FRPLR2  1280  // Right  Boundary of Bottom−Left
FRPLL2  870   // Left   Boundary of Bottom−Left
FRPLT2  935   // Top    Boundary of Bottom−Left
FRPLB2  510   // Bottom Boundary of Bottom−Left

NHDR2  432      // Number of Lines in the Header Part
NHDR   432      //360   // Number of Lines in the Header Part
                // 432 for the data in April 2012
                // 360 for Most Images
                // 252 for Images of Very Early SEEDS
```

Appendix B

MCFOST Parameter Files

B.1 Single Disk Model

```
2.17                         mcfost version

#Number of photon packages
  1e8                     nbr_photons_eq_th   : T computation
  1e4                nbr_photons_lambda : SED computation
  1e8                     nbr_photons_image   : images computation

#Wavelength
  100   0.1  3000.0            n_lambda, lambda_min, lambda_max [mum]
  T T F                      compute temperature?, compute sed?, use default wavelength grid ?
  robin.lambda               wavelength file (if previous parameter is F)
  F T                        separation of different contributions?, stokes parameters?

#Grid geometry and size
  1                          1 = cylindrical, 2 = spherical
  150 70 1 10                n_rad (log distribution), nz (or n_theta), n_az, n_rad_in

#Maps
  511 511 898.1   1.0        grid (nx,ny), size [AU], zoom factor
  10    1    1              MC : N_bin_incl, N_bin_az
  31.74   31.74   1   F          RT: imin, imax, n_incl, centered ?
  185.0                      distance (pc)
  33.9                       disk PA

#Scattering method
  0                          0=auto, 1=grain prop, 2=cell prop
  1                          1=Mie, 2=hg (2 implies the loss of polarization)

#Symetries
  T                          image symmetry
  T                          central symmetry
  T                          axial symmetry (important only if N_phi > 1)
```

```
#Dust global properties
  1      0.00   0.5          dust_settling (0=no settling, 1=parametric, 2=Dubrulle, 3=Fromang), exp_strat, a_strat (for parametric settling)
  F                          sublimate dust
  F  0.0                     viscous heating, alpha_viscosity

#Number of zones : 1 zone = 1 density structure + corresponding grain properties
  1

#Density structure
  1                          zone type : 1 = disk, 2 = tappered-edge disk, 3 = envelope, 4 = wall
  7.e-4    100.              dust mass,  gas-to-dust mass ratio
  3.5  100.0                 scale height, reference radius (AU), unused for envelope
  2.7   92.0 0.00           Rin, Rout (or Rc), edge (AU)
  1.3                       flaring exponent, unused for envelope
  -1.5  0.0                  surface density exponent (or -gamma for tappered-edge disk or volume density for envelope), usually < 0, -gamma_exp

#Cavity : everything is empty above the surface
 F                           cavity ?
 10. 50.                     height, reference radius (AU)
 1.5                         flaring exponent

#Grain properties
  1  Number of species
  Mie  1 2   0.0   1.0   0.9 Grain type (Mie or DHS), N_components, mixing rule (1 = EMT or 2 = coating),  porosity, mass fraction, Vmax (for DHS)
  Draine_Si_sUV.dat  1.0     Optical indices file, volume fraction
  1                          Heating method : 1 = RE + LTE, 2 = RE + NLTE, 3 = NRE
  0.005  1000.0 3.5 50       amin, amax [mum], aexp, n_grains (log distribution)

#Molecular RT settings
  T T T 15.                  lpop, laccurate_pop, LTE, profile width (km.s^-1)
  0.2                        v_turb (delta)
  2                          nmol
  13co@xpol.dat 6               molecular data filename, level_max
  1.0 50                     vmax (km.s^-1), n_speed
  T 1.e-6 abundance.fits.gz    cst molecule abundance ?, abundance, abundance file
  T  3                          ray tracing ?,  number of lines in ray-tracing
  1 2 3                      transition numbers
  co@xpol.dat 6              molecular data filename, level_max
  1.0 50                     vmax (km.s^-1), n_speed
```

```
  T 1.e-6 abundance.fits.gz    cst molecule abundance ?, abundance,
      abundance file
  T  3                         ray tracing ?,  number of lines in ray-
      tracing
  1 2 3                      transition numbers

#Star properties
  1 Number of stars
  4200.0          2.16     1.10     0.0      0.0      0.0  F Temp, radius (
      solar radius),M (solar mass),x,y,z (AU), is a blackbody?
  lte4200-3.5.NextGen.fits.gz
  0.0    2.2  fUV, slope_fUV
```

B.2 Multi-zone Model

```
2.17                        mcfost version

#Number of photon packages
  1e8                   nbr_photons_eq_th   : T computation
  1e4                     nbr_photons_lambda : SED computation
  1e8                 nbr_photons_image   : images computation

#Wavelength
  100   0.1  3000.0            n_lambda, lambda_min, lambda_max [mum]
  T T F                     compute temperature?, compute sed?, use default wavelength grid ?
  robin.lambda              wavelength file (if previous parameter is F)
  F T                       separation of different contributions?, stokes parameters?

#Grid geometry and size
  1                         1 = cylindrical, 2 = spherical
  150  70  1  10            n_rad (log distribution), nz (or n_theta), n_az, n_rad_in

#Maps
  511  511  898.1   1.0       grid (nx,ny), size [AU], zoom factor
  10    1    1               MC : N_bin_incl, N_bin_az
  31.74   31.74   1   F          RT: imin, imax, n_incl, centered ?
  185.0                     distance (pc)
  37.0                      disk PA

#Scattering method
  0                         0=auto, 1=grain prop, 2=cell prop
  1                         1=Mie, 2=hg (2 implies the loss of polarization)

#Symetries
  T                         image symmetry
  T                         central symmetry
  T                         axial symmetry (important only if N_phi > 1)

#Dust global properties
  0      0.20   1.0         dust_settling (0=no settling, 1=parametric, 2=Dubrulle, 3=Fromang), exp_strat, a_strat (for parametric settling)
  F                         sublimate dust
  F   0.0                   viscous heating, alpha_viscosity

#Number of zones : 1 zone = 1 density structure + corresponding grain properties
  4

#Density structure
  1                         zone type : 1 = disk, 2 = tappered-edge disk, 3 = envelope, 4 = wall
```

```
2.06E-9 100.            dust mass,  gas-to-dust mass ratio
3.4   100.0              scale height, reference radius (AU), unused for envelope
0.5   10.0   0.00      Rin, Rout (or Rc), edge (AU)
1.25                     flaring exponent, unused for envelope
-1.0   -1.0             surface density exponent (or -gamma for tappered-edge disk or volume density for envelope), usually < 0, -gamma_exp

1                       zone type : 1 = disk, 2 = tappered-edge disk, 3 = envelope, 4 = wall
1.10E-8 100.            dust mass,  gas-to-dust mass ratio
2.0   30.0              scale height, reference radius (AU), unused for envelope
30.0   30.1   0.00      Rin, Rout (or Rc), edge (AU)
1.25                     flaring exponent, unused for envelope
-1.0   -1.0             surface density exponent (or -gamma for tappered-edge disk or volume density for envelope), usually < 0, -gamma_exp

2                       zone type : 1 = disk, 2 = tappered-edge disk, 3 = envelope, 4 = wall
1.90E-4  100.           dust mass,  gas-to-dust mass ratio
3.4   100.0              scale height, reference radius (AU), unused for envelope
30.1   115.0   0.00       Rin, Rout (or Rc), edge (AU)
1.25                    flaring exponent, unused for envelope
-1.0   -1.0             surface density exponent (or -gamma for tappered-edge disk or volume density for envelope), usually < 0, -gamma_exp

2                       zone type : 1 = disk, 2 = tappered-edge disk, 3 = envelope, 4 = wall
1.08E-3  100.           dust mass,  gas-to-dust mass ratio
0.68   100.0              scale height, reference radius (AU), unused for envelope
30.1   115.0   0.00       Rin, Rout (or Rc), edge (AU)
1.25                    flaring exponent, unused for envelope
-1.0   -1.0             surface density exponent (or -gamma for tappered-edge disk or volume density for envelope), usually < 0, -gamma_exp

#Cavity : everything is empty above the surface
F                       cavity ?
10. 50.                 height, reference radius (AU)
1.1                     flaring exponent

#Grain properties
 1  Number of species
 Mie   1 2   0.0   1.0   0.9 Grain type (Mie or DHS), N_components, mixing rule (1 = EMT or 2 = coating),  porosity, mass fraction, Vmax (for DHS)
 Draine_Si_sUV.dat  1.0  Optical indices file, volume fraction
```

```
1                         Heating method : 1 = RE + LTE, 2 = RE + NLTE, 3 = NRE
0.005  0.25  3.5  50      amin, amax [mum], aexp, n_grains (log distribution)

1  Number of species
Mie  1 2  0.0  1.0  0.9 Grain type (Mie or DHS), N_components, mixing rule (1 = EMT or 2 = coating),  porosity, mass fraction, Vmax (for DHS)
Draine_Si_sUV.dat  1.0  Optical indices file, volume fraction
1                       Heating method : 1 = RE + LTE, 2 = RE + NLTE, 3 = NRE
0.005  0.25  3.5  50    amin, amax [mum], aexp, n_grains (log distribution)

1  Number of species
Mie  1 2  0.0  1.0  0.9 Grain type (Mie or DHS), N_components, mixing rule (1 = EMT or 2 = coating),  porosity, mass fraction, Vmax (for DHS)
Draine_Si_sUV.dat  1.0  Optical indices file, volume fraction
1                       Heating method : 1 = RE + LTE, 2 = RE + NLTE, 3 = NRE
0.005  1.  3.5  50      amin, amax [mum], aexp, n_grains (log distribution)

1  Number of species
Mie  1 2  0.0  1.0  0.9 Grain type (Mie or DHS), N_components, mixing rule (1 = EMT or 2 = coating),  porosity, mass fraction, Vmax (for DHS)
Draine_Si_sUV.dat  1.0  Optical indices file, volume fraction
1                       Heating method : 1 = RE + LTE, 2 = RE + NLTE, 3 = NRE
0.005  1000.  3.5  50           amin, amax [mum], aexp, n_grains (log distribution)

#Molecular RT settings
T T T 15.               lpop, laccurate_pop, LTE, profile width (km.s^-1)
0.2                     v_turb (delta)
2                       nmol
13co@xpol.dat 6           molecular data filename, level_max
1.0 50                  vmax (km.s^-1), n_speed
T 1.e-6 abundance.fits.gz   cst molecule abundance ?, abundance, abundance file
T  3                        ray tracing ?,  number of lines in ray-tracing
1 2 3                   transition numbers
co@xpol.dat 6           molecular data filename, level_max
1.0 50                  vmax (km.s^-1), n_speed
T 1.e-6 abundance.fits.gz   cst molecule abundance ?, abundance, abundance file
T  3                        ray tracing ?,  number of lines in ray-tracing
1 2 3                   transition numbers
```

```
#Star properties
  1 Number of stars
  4200    2.16   1.10   0.0   0.0   0.0   F Temp, radius (solar radius),M (
      solar mass),x,y,z (AU), is a blackbody?
  lte4200-3.5.NextGen.fits.gz
  0.00   2.2   fUV, slope_fUV
```